# An Enhanced SD-GS-AL Algorithm for Coordinating the Optimal Power and Traffic Flows With EVs

Santosh Sharma<sup>©</sup>, Student Member, IEEE, Qifeng Li<sup>©</sup>, Senior Member, IEEE, and Wei Wei<sup>10</sup>, Senior Member, IEEE

Abstract—The electric power distribution network (PDN) and the transportation network (TN) are generally operated/coordinated by different entities. However, they are coupled through electric vehicle charging stations (EVCSs). This paper proposes to coordinate the operation of the two systems via a fully decentralized framework where the PDN and TN operators solve their own operation problems independently, with only limited information exchange. Nevertheless, the operation problems of both systems are generally mixed-integer programs (MIP), for which mature algorithms like the alternating direction method of multipliers (ADMM) may not guarantee convergence. This paper applies a novel distributed optimization algorithm called the SD-GS-AL method, which is a combination of the simplicial decomposition, gauss-seidel, and augmented Lagrangian, which can guarantee convergence and optimality for MIPs. However, the original SD-GS-AL may be computationally inefficient for solving a complex engineering problem like the PDN-TN coordinated optimization investigated in this paper. To improve the computational efficiency, an enhanced SD-GS-AL method is proposed by redesigning the inner loop of the algorithm, which can automatically and intelligently determine the iteration number of the inner loop. Simulations on the test cases show the efficiency and efficacy of the proposed framework and algorithm.

Index Terms—Decentralized algorithms, mixed-integer programs, optimal power-traffic flow.

# Nomenclature

Indices, Superscripts, Subscripts and Sets: TN Model

$\boldsymbol{A}$	Set of arcs in the traffic network
a	Index for arcs in the traffic network
ev	Superscript for EV
evcs	Superscript for EVCS
m, n	Index for nodes in the traffic network
N	Set of nodes in the traffic network
$O_{rs}$	Path set of O-D pair rs

Manuscript received 20 August 2023; revised 25 November 2023; accepted 16 January 2024. Date of publication 26 January 2024; date of current version 21 June 2024. The work of Santosh Sharma and Qifeng Li was supported by the U.S. National Science Foundation under Award CBET 2124849. Paper no. TSG-01325-2023. (Corresponding author: Qifeng Li.)

Santosh Sharma and Qifeng Li are with the Department of Electrical Engineering, University of Central Florida, Orlando, FL 32826 USA (e-mail: qifeng.li@ucf.edu).

Wei Wei is with the State Key Laboratory of Power Systems, Department of Electrical Engineering, Tsinghua University, Beijing 100084, China.

Color versions of one or more figures in this article are available at https://doi.org/10.1109/TSG.2024.3358805.

Digital Object Identifier 10.1109/TSG.2024.3358805

Index for path in the traffic network

Index for O-D pairs

Indices and Sets: Enhanced SD-GS-AL

CH(.) Convex hull  $CH(X_p)$ Convex hull of  $X_n$ 

Mixed-integer convex set of dOPF Mixed-integer convex set of OTF

Parameters: PDN Model

Squared of current carrying capacity of line ik  $\overline{\ell}_{ik}$ 

 $\overline{S}_{ik}$ MVA limit of line ik

Minimum and maximum voltage limits

Grid electricity price

Active, reactive power demand due to EVCS at

Active, reactive power demand at node i Active, reactive power output from solar PV at

Resistance and reactance of line ik  $r_{ik}, x_{ik}$ 

# Parameters: TN Model

$\beta^{rs}$	Energy consumption ratio of EV
$\delta_a^q$	Binary variable to identify arcs of path $q$
$\lambda_m$	Electricity price for charging at node <i>m</i>
$\mathbf{I}^{rs}$	Vector for origin and destination nodes of rs
$b_{m,max}$	Availability of EVCS at node m
$d_a$	Travelling distance of arc a
	Initial battery energy of an EV
$E_0^{rs}$ $e_{init}^q$	Battery energy of EV at initial node of path q
$E_{min}^{rs}, E_{max}^{rs}$	Minimum, maximum energy capacity of EV
$F^{rs}$	Travel demand of O-D pair rs
$P_m^{pile}$	Rated power of EV charging piles at node m
$P_{m,max}^{evcs}$	Maximum power output of EVCS at node <i>m</i>
$R^{rs}$	Mile anxiety of EV
$t_a^0, c_a$	Parameters for travel time function of arc a
$t_a^0, c_a$ $t_m^0, \alpha_m$	Parameters for waiting time in EVCS at node
m.	m
$tan\phi_m^{evcs}$	Power factor of EVCS at node m

Weighting factor from time to monetary cost

K Node-arc incidence matrix

1949-3053 © 2024 IEEE. Personal use is permitted, but republication/redistribution requires IEEE permission. See https://www.ieee.org/publications/rights/index.html for more information.

Parameters: Enhanced SD-GS-AL

$\epsilon_{\mathrm{u}}$	Convergence	tolerance	of	inner	loop
-------------------------	-------------	-----------	----	-------	------

 $\epsilon/\epsilon_{\rm u}$  Convergence tolerance  $\gamma$  Penalty parameter

J Maximum number of inner loop iterationsK Maximum number of outer loop iterations

#### Variables: PDN Model

$\ell_{ik}$	Squared of current flow on line ik
$p_{i,t}^{\mathrm{G}}, \boldsymbol{p^{\mathrm{G}}}$	Grid power purchased
$p_{ik}, q_{ik}$	Active, reactive power flow on line ik
$p_i^{G}, q_i^{G}$	Active and reactive power from grid at node i
$v_i$	Squared of voltage at node i

#### Variables: TN Model

$\gamma_m^q$	0-1 charging choice at node <i>m</i>		
$C_q^{rs} \ C^{rs}$	Travel cost of path q		
	Travel cost of O-D pair rs		
$E_m^q$	Charging energy of EV at node at node m		
$e_m^{"}$	Remaining battery energy of EV at node m		
$e_{init}^q$ Battery energy of EV at initial node of p			
$f_{rs}^{q}$	Traffic flow rate on path $q$ of O-D pair $rs$		
$e_{init}^{q}$ $f_{rs}^{q}$ $p_{m}^{\mathrm{T}}, q_{m}^{\mathrm{T}}$	Active, reactive power demand of EVCS at		
	node m		
$t_a$	Travel time on arc a		
$t_m$	Charging time at node m		
$x_a$	Traffic flow rate on arc a		
$x_m$	Traffic flow rate at node $m$		

#### Variables: Enhanced SD-GS-AL

$x_{\mathbf{v}}$	OTF decision variables
$x_{\mathbf{p}}$	dOPF decision variables
$\check{arphi}_{ m p}$	Lagrangian lower bound of power subproblem
$egin{array}{c} oldsymbol{x_p} \ oldsymbol{\check{arphi}_p} \ oldsymbol{\check{arphi}_V} \end{array}$	Lagrangian lower bound of transportation sub-
	problem
$\hat{arphi}_{ extsf{p}}$	Lagrangian upper bound of power subproblem
$\hat{arphi}_{ m p} \ \hat{arphi}_{ m v}$	Lagrangian upper bound of transportation sub-
	problem
$\lambda_p \backslash \lambda_v$	Lagrangian multipliers
<i>z</i> .	Auxiliary variable

#### I. INTRODUCTION

DUE TO the increasing concern over carbon emissions, electric vehicles (EVs) are gradually replacing fossilfueled vehicles [1]. It is predicted that by 2030, the number of EVs on the road will exceed 100 million, a massive increase from the 5.1 million present in 2019. The widespread adoption of EVs will lead to a significant increase in the electricity demand on power distribution networks (PDNs) for EV charging. This poses a high risk of PDN overloading during peak-demand hours. Furthermore, the locations of EV charging stations (EVCSs) along transportation networks (TNs) can have an impact on the routes and travel times of EVs that require charging. To mitigate the negative effects of large-scale EV charging on PDNs and alleviate potential traffic congestion in TNs, proper EV routing along TNs and charging schedules

are necessary. As a result, proper coordination between the operation of EVs-infused transportation and power distribution networks is vital to ensure the seamless adoption of large-scale EVs.

In recent times, several studies have been conducted to improve the efficiency and reliability of TNs and PDNs by coordinating their operations. One such proposal put forth by the authors in [2] suggests a centralized optimal traffic-power flow for routing EVs in electrified TN, which has been further extended to accommodate time-varying electricity prices and traffic demands in [3]. The traffic flow is modeled using a semi-dynamic traffic assignment technique that accounts for flow propagation between adjacent periods. Meanwhile, [4] introduces a bilevel optimization model that allows EV aggregators to participate in day-ahead dispatch while adhering to various system operation constraints. Additionally, [5] proposes a centralized model for a dynamic pricing strategy for integrated electricity charging and hydrogen refueling stations (IEHSs) that guides the charging and refueling decisions of different EV types and ensures the smooth operation of IEHSs, the power distribution network, and the gas network. Likewise, [6] proposes a dynamic pricing strategy for an EV charging station that maximizes net charging profits by incorporating the behavior of EV drivers based on both an admission control scheme and a queuing model.

However, there is a common issue associated with the above-mentioned studies: they all considered a centralized operational framework. Since transportation and power distribution systems are operated by different entities, and there is no entity that has access to both TN and PDN information, implementing a centralized model of operation may not be practical due to privacy concerns and communication overhead. The TN coordinator (TNC) has the responsibility of solving the optimal traffic flow (OTF) for EVs [2], which involves identifying the most efficient routing and charging schedule for electric vehicles (EVs). On the other hand, the task of the power distribution system operator (P-DSO) is to operate the power distribution network by solving the distribution-level optimal power flow (dOPF) problem [7]. Since electric vehicle charging stations (EVCSs) are powered by power distribution networks (PDNs), TNs and PDNs are physically connected. The variables that are common to both OTF and dOPF are called boundary variables (i.e., charging loads of EVCSs). If OTF and dOPF are solved independently without coordination, boundary variables may not match, resulting in an insecure or sub-optimal performance of both systems.

After realizing this issue, researchers have proposed decentralized frameworks to coordinate TNs and PDNs with EVs. These frameworks involve obtaining the routes of EVs using the best response decomposition (BRD) algorithm [8], coordination of hydrogen-integrated TN and PDNs using the alternating direction method of multipliers (ADMM) [9], a novel optimal traffic power flow problem via an extended ADMM to analyze the spatial and temporal congestion propagation on coupled transportation power systems under congested roads, transmission lines and charging stations [10], multistage distributionally robust optimization

model to address wind power uncertainty based on improved ADMM [11], coordination of the charging schedule of EVs and stochastic security-constrained unit commitment using the bender decomposition method (BDM) [12], augmented Lagrangian alternating direction inexact newton (ALADIN) based coordination for time-varying traffic demands and intertemporal EV charging behavior [13], an improved fixed-point algorithm (FPA) based on extrapolation for the spatial and temporal evolution of traffic flows [14]. Similarly, other frameworks include stochastic user equilibrium traffic assignment using optimality condition decomposition (OCD) method [15], strategic pricing method to maximize the profit of EVCS owners using Karush-Kuhn-Tucker (KKT) condition [16], the generalized user equilibrium method for the coupled powertransportation network operation using a master and a series of subproblems (MSS) approach [17], a new collaborative pricing model for the power-transportation coupled network based on a variational inequality approach using an improved prediction-correction algorithm (IPCA) [18], the iterative column generation (CG) algorithm to explicitly describe PEVs' driving range constraints on TNs [19].

Moreover, other decentralized optimization-based frameworks to coordinate PDN and TN involve the multi-agent system framework utilizing consensus algorithms for a realtime navigation system for EV drivers, optimizing both time and cost by considering traffic conditions and power distribution, to guide drivers to the most efficient charging stations [20], Stackelberg game based iterative approach for day-ahead scheduling framework for electric vehicles integrating grid-to-vehicle and vehicle-to-grid services [21], optimistic iterative algorithm and simulated annealing for capturing the interconnected decisions of TN and PDN operators due to Electric Vehicles' (EVs) actions [22], game theory based multiagent approach to model the competitive pricing strategies of individually-owned EV charging stations in urban transportation networks, aiming to determine optimal charging prices [23], combined consensus and generalized benders decomposition algorithms for collaborative optimal routing and scheduling method for EVs that unifies navigation services in the transportation network with power scheduling in the distribution network, improving traffic flow, charging facility utilization, and charging economy [24], and CG based approach for competitive pricing of EVCSs, considering both competition and the impact on distribution locational marginal price [25].

To simulate the routing and charging schedule of EVs in TN, binary variables are employed, making OTF a mixed-integer program [8]. Likewise, binary variables are used to capture the behavior of switched capacitors and voltage regulators in dOPF, thereby rendering the dOPF a mixed-integer program too [26]. Nevertheless, the decentralized algorithms mentioned above exhibit at least one of the following primary issues: First, they do not provide a guarantee of optimality and convergence for mixed-integer programs (MIPs), such as OTF and dOPF. For instance, the BRD, ADMM, BDM, OCD, KKT, CG, and IPCA algorithms can only ensure optimality and convergence for convex problems. Second, some of these algorithms, e.g., BRD and MSS, require TNC and P-DSO to

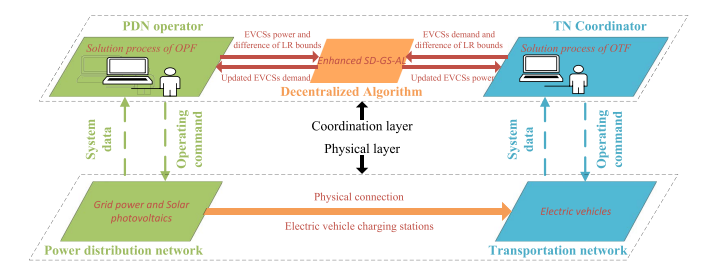


Fig. 1. Proposed framework for the decentralized coordination of PDN and TN

exchange a significant amount of information, which results in high investment in building communication channels and causes long communication delays. Additionally, TNC and P-DSO may not want to share their confidential information. Third, some of these algorithms, such as ALADIN and MSS, are not fully decentralized as they require certain steps (such as updating the Hessian matrix and solving the master subproblem) to be performed by a central coordinator (which may not be practical in a purely decentralized environment).

Beyond the decentralized coordination of PDN and TN, there is a broad interest across power systems for a decentralized optimization algorithm applicable for mixed-integer programs [27]. Some examples include the coordinated operation of the water-energy nexus, the coordinated operation and restoration of power transmission and distribution systems, and the integrated operation of power and gas networks. Most commonly used decentralized optimization algorithms in popular power system applications can be broadly categorized into three types [27]: a) the Lagrangian relaxation-based methods such as dual decomposition, ADMM, ALADIN, analytical target cascading (ATC) [28], auxiliary problem principle (APP) [29], and proximal message passing (PMP) [30]; b) the Karush-Kuhn-Tucker (KKT) conditions based methods such as OCD, consensus algorithms, and heterogeneous decomposition (HGD), and c) the benders decomposition (BD) methods such as MSS. Nevertheless, as with previously mentioned algorithms, these algorithms may not always work for subproblems that contain integer variables. Therefore, there is a need for a fully decentralized algorithm that facilitates the coordination of MIP problems such as OTF and dOPF with limited information exchange, as shown in Figure 1.

Recently, a promising algorithm called the SD-GS-AL algorithm [31], which is a combination of the simplicial decomposition, gauss-seidel, and augmented Lagrangian, has been shown to guarantee optimality and convergence to MIP subproblems if the number of inner loop iterations is set to be big enough. However, a large number of inner loop iterations results in a high computational burden, which makes the SD-GS-AL algorithm computationally inefficient for problems like the PDN-TN coordinated optimization. To be precise, in the original SD-GS-AL algorithm, the number of inner loops is set by the user in advance based on experience. If the number of inner loop iterations is set too high, the algorithm becomes computationally inefficient. If the number of inner loop iterations is set too low, the algorithm may not converge. To mitigate this issue, we propose an enhanced SD-GS-AL decentralized algorithm by redesigning the inner loop of the

(2b)

algorithm, which can automatically and intelligently determine the iteration number of the inner loop. The main contributions can be summarized as follows:

- 1) From the engineering perspective, this research respects the fact that the two systems are operated by different operators and proposes to coordinate the two systems via a new decentralized method, i.e., the enhanced SD-GS-AL algorithm. The proposed method has the following benefits: a) it is applicable to MIP problems with convergence and optimality guaranteed under mild assumptions (i.e., (1) the global optimal solution of the coordinated dOPF-OTF is unique, (2) the objective function is linear, and (3) the constraint sets are in mixed-integer convex program (MICP) forms), b) it only requires limited information exchange between PDN and TN operators, which will help preserve the privacy of the two systems and reduce the investment in building communication channels, and c) it is fully decentralized so that all the computations (i.e., optimizations) are carried out in parallel by PDN operator and TN coordinator only.
- 2) From the perspective of mathematical method, being different from the original SD-GS-AL algorithm [31], the redesigned inner loop can automatically and intelligently terminate the inner loop iterations, which significantly improves the computational efficiency of the overall algorithm. Note that the proposed algorithm is general and applicable to other problems that have similar features.

#### II. PROBLEM FORMULATION

# A. Power Distribution Network Model

Distributed energy resources (DERs), like solar photovoltaics (PVs), and grid power, which supply EVCSs in the transportation network and other loads in the power distribution network, are considered in this paper. The resulting distribution system model is given as follows [32]:

$$(p_{ik})^2 + (q_{ik})^2 = v_i \ell_{ik}$$
 (1a)

 $v_i - v_k - 2(r_{ik}p_{ik} + x_{ik}q_{ik})$ 

$$+ ((r_{ik})^2 + (x_{ik})^2)\ell_{ik} = 0$$
 (1b)

$$0 \le \ell_{ik} \le \overline{\ell}_{ik} \tag{1c}$$

$$(p_{ik})^2 + (q_{ik})^2 \le (\overline{S}_{ik})^2$$
 (1d)

$$\left(\underline{v}_i\right)^2 \le v_i \le (\overline{v}_i)^2 \tag{1e}$$

$$p_i^{G} + p_i^{PV} - p_i^{Load} - p_i^{D} = \sum_j (p_{ji} - r_{ji}\ell_{ji}) + \sum_k p_{ik}$$
(1f)

$$q_i^{\text{G}} + q_i^{\text{PV}} - q_i^{\text{Load}} - q_i^{\text{D}} = \sum_{j} (q_{ji} - x_{ji}\ell_{ji}) + \sum_{k} q_{ik}(1g)$$

$$q_i^{\rm D} = p_i^{\rm D} tan(\theta_i^{\rm D}). \tag{1h}$$

The balanced power flows are modeled using the *DistFlow* model [32], which is expressed in equation (1a). The distribution line connecting nodes i(j) and k(i) is denoted by the index ik(ji). The voltage drop on a distribution line is constrained by equation (1b), while the thermal and power carrying limits of

distribution lines are given by constraints (1c) and (1d), respectively. The voltage limits are specified by constraint (1e). The nodal active and reactive power balance equations are given by constraints (1f) and (1g), respectively. The constraint (1h) represents the reactive power demand due to the EVCSs, where  $\theta_i^D$  is the power factor angle (is assumed fixed) of the EVCS. Throughout the paper, **bold** symbols denote matrices/vectors of corresponding variables.

#### B. Transportation Network Model

In this subsection, we briefly provide a description of the adopted model of the traffic flow for EVs. For a detailed understanding of the model, readers are referred to [17]. The transportation network (TN) is represented by a directed graph G = [N, A], where N and A refer to the set of nodes and arcs, respectively. To specify electric vehicle (EV) travel and charging options, a path is formed by combining nodes and arcs. The nodes correspond to the starting and ending points of an arc, junctions, and charging stations for EVs, while arcs connect two nodes. Even though the traffic network will have both electric and non-electric vehicles, we consider routing and charging of only electric vehicles in this paper as in [17]. Therefore, the traffic parameters used in this paper are non-electric vehicles discounted. The resulting model is given as follows:

$$\mathbf{K}\delta_a^q = \mathbf{I}^{rs}$$

$$-M(1 - \delta_a^q) \le e_m^q - e_n^q + d_a \beta^{rs} - E_m^q$$
(2a)

$$= M(1 - \delta_a) \le \epsilon_m - \epsilon_n + u_a p - L_m$$

$$\le M(1 - \delta_a^q), \forall (n, m) = a \in A$$

$$e_n^q - d_a \beta^{rs} \ge -M(1 - \delta_a^q) + R^{rs} E_{max}^{rs},$$

$$\forall (n, m) = a \in A \tag{2c}$$

$$E_m^q \le b_{m,max}, \forall m \in N$$
 (2d)

$$E_m^q \le \gamma_m^q E_{max}^{rs} \le e_m^q, \forall m \in N$$
 (2e)

$$e_{init}^q = E_0^{rs} \tag{2f}$$

$$E_{min}^{rs} \le e_m^q \le E_{max}^{rs}, \forall m \in N$$
 (2g)

$$t_a = t_a^0 (1 + 0.15(x_a/c_a)^4), \forall a \in A$$
 (2h)

$$t_m = t_m^0 (1 + \alpha_m x_m), \forall m \in N$$
 (2i)

$$0 \le f_q^{rs} \perp \left(C_q^{rs} - C_{rs}\right) \ge 0, \forall q \in O_{rs}$$
 (2j)

$$\sum_{q \in O_{rs}} f_q^{rs} = F^{rs}, \forall rs$$
 (2k)

$$x_a = \sum_{rs} \sum_{q \in O} f_q^{rs} \delta_a^q, \forall a \in A$$
 (21)

$$x_m = \sum_{rs} \sum_{q \in O} f_q^{rs} \gamma_m^q, \forall m \in N$$
 (2m)

$$C_q^{rs} = w \left( \sum_a t_a \delta_a^q + \sum_m \left( E_m^q / P_m^{pile} + t_m \gamma_m^q \right) \right) + \sum_m E_m^q \lambda_m, \forall q, \forall rs$$
 (2n)

Constraint (2a) specifies the starting and ending nodes of path q for an origin-destination (O-D) pair rs. Note that the vector  $\mathbf{I}^{rs}$  consists of two non-zero elements of 1 and -1 at the

origin and the destination nodes of O-D pair rs, respectively. Constraint (2b) tracks the dynamics of the energy stored in the EVs, denoted by  $e_m^q$ , and the charging energy at nodes, denoted by  $E_m^q$ . The EV energy consumption ratio is denoted by  $\beta^{rs}$ , and the binary variable  $\gamma_m^q$  indicates whether an EV along path q is charged at node m. A very large positive constant M is a Big-M parameter. Constraint (2c) accounts for the range anxiety of EVs for O-D pair rs, represented by  $R^{rs}$ , where  $E_{max}^{rs}$  is the maximum energy that an EV for O-D pair rs can store. Constraint (2d) specifies the charging behavior of EVs, where  $b_{m,max}$  is set to 0 if there is no EV charging station (EVCS) at node m. Constraint (2e) ensures that the EVs are fully charged after each charging cycle, which is a realistic assumption as EV drivers tend to minimize the frequency of charging. Constraints (2f) and (2g) impose limits on the initial energy stored  $(E_0^{rs})$  in the EVs and the maximum energy (and minimum energy,  $E_{min}^{rs}$ ) that can be stored in their batteries, respectively.

The function  $t_a(x_a)$  in equation (2h), based on the commonly used Bureau of Public Roads (BPR) function [33], represents travel time on arc a, where  $x_a$  is the traffic flow on arc a. The function  $t_m(x_m)$  in equation (2i) describes the time required for charging and waiting for service at EVCSs, where  $x_m$  is node traffic flow. The charging time is dependent on the rated power of the charging station  $P_m^{pile}$ , while the waiting time is represented by  $t_m^0$ , which is fixed and is affected by the level of congestion in EV charging stations (EVCSs), estimated by  $\alpha_m$ . To account for congestion in the power grid at different locations, the electricity price  $\lambda_m$  at an EVCS node m is given by the distribution locational marginal price (DLMP) of the corresponding location in PDN, and more information on how to obtain  $\lambda_m$  will be provided later when we introduce the algorithm. The traffic equilibrium condition is described by constraint (2j), which states that the travel cost  $C^{rs}$  for origin-destination (O-D) pair rs should be equal for all used paths and no greater than that for any unused path. This condition is also known as the Wardrop User Equilibrium (UE) Principle [34]. The variable  $f_q^{rs}$  represents EV flow on path q for O-D pair rs. Constraint (2k) represents the conservation of traffic flow. In constraints (21) and (2m), the mathematical expression for arc flow  $x_a$  and node flow  $x_m$  is provided. Constraint (2n) provides the expression for the total cost ( $C_a^{rs}$ ) of path q for an O-D pair rs, which includes travel time, charging time for EVs, and the charging cost for EVs.

Note that this paper considers the static Traffic Assignment Problem (TAP), which is the foundation for dynamic traffic assignment. However, the dynamic TAP is more complex than the static TAP, and there is no universally accepted model available for it [17]. Moreover, the existing literature that considers the coordination of PDN and TN with EVs mostly uses static TAP for optimal coordination [17]. Nonetheless, the proposed framework and algorithms would work for a dynamic TAP if they were available.

# C. Coupling Between PDN and TN

From a system-level perspective, on-road fast charging stations would simultaneously impact vehicle routing in the transportation system, and power flows in the distribution system, therefore, tightly coupling the two systems. Mathematically, the coupling between PDN and TN can be captured as follows:

$$p_m^{\mathsf{T}} = \sum_{rs} \sum_{q \in O_{rs}} f_q^{rs} E_m^q, \forall m \in \mathbb{N}$$

$$0 \le p_m^{\mathsf{T}} \le p_{m,max}^{\mathsf{T}}, \forall m \in \mathbb{N}$$
(3a)

$$0 \le p_m^{\mathrm{T}} \le p_{m,max}^{\mathrm{T}}, \forall m \in N \tag{3b}$$

where  $p_m^{\rm T}$  is the power consumption of EVs in TN and acts as a power demand to PDN. The constraint (3a) is the active power consumed at the EVCSs, while (3b) provides the capacity limit of EVCSs.

# D. Convexification and Linearization of Non-Linear Constraints

The PDN model (1) is a non-linear programming (NLP) problem due to the non-linear non-convex constraint (1a). Similarly, the TN model (2) is in mixed-integer non-linear programming (MINLP) form due to the non-linear BPR function (2h) and bilinear traffic equilibrium constraint (2j). In addition, the coupling constraint (3a) is non-linear due to the multiplication of two continuous variables. Reference [32] found that, if one can find the tight convex relaxation for MINLP form, the solution of the mixed-integer convex program (MICP) form of the dOPF model (1) coincides with the solutions of the MINLP form but with a reduced computational burden. Therefore, in this paper, we employ the convex hull relaxation from [32], [35] for (1a) and piece-wise linearization techniques from [36] for (2h) and (2j). For accuracy of the convex hull relaxation and the piece-wise linearization, readers are referred to [35] and [36], respectively. The convex hulls relaxation of (1a) is given as follows:

$$p_{ik}^2 + q_{ik}^2 \le v_i \ell_{ik}$$

$$\overline{S}_{ik}^2 v_i + v_i \overline{v}_i \ \ell_{ik} \le \overline{S}_{ik}^2 (v_i + \overline{v}_i).$$
(4a)

$$\overline{S}_{ik}^2 v_i + \underline{v}_i \overline{v}_i \ \ell_{ik} \le \overline{S}_{ik}^2 (\underline{v}_i + \overline{v}_i). \tag{4b}$$

Note that the conic relaxation (4a) and the expression (4b) collectively represent the convex hulls relaxation of (1a).

The BPR function constraint (2h) is a non-linear constraint, which is approximated by a piecewise linearization technique using a special ordered set of type-2 (SOS2) variables [36]. In piecewise linearization, the non-linear function is divided into a number of segments, and each segment is represented by a linear function. The piecewise linearization of the BPR function constraint (2h) is given as follows:

$$x_a = \sum_{n} x_a^n y_a^n; \ t_a = \sum_{n} t_a^n (x_a^n) y_a^n$$
 (5a)

$$\sum_{n} y_{a}^{n} = 1; \ 0 \le \{y_{a}^{n}, \forall n\} \in SOS2, \tag{5b}$$

where  $x_a^n$  and  $t_a^n$  denote the values of  $x_a$  and  $t_a$ , respectively, while  $y_a^n$  is a vector of SOS2 variables, in which at most two adjacent variables can be nonzero. The user equilibrium constraint (2j) is a bilinear constraint, which is linearized using the Big-M method as follows:

$$0 \le f_q^{rs} \le M v_q^{rs}, \forall q, rs \tag{6a}$$

$$0 \le C_q^{rs} - C^{rs} \le M\left(1 - \nu_q^{rs}\right), \forall q, \forall rs, \tag{6b}$$

where,  $v_a^{rs}$  is a binary variable for each path. The coupling constraint (3a) is also a non-linear constraint. The same piecewise linearization technique, used in (5), is applicable for the linearization of (3a). Owing to the page limit, the detailed modeling is omitted. Finally, the convex constraints set of PDN, denoted by  $\mathcal{X}_p$ , is defined as follows:

$$\mathcal{X}_{p} := \{ (1b) - (1h), (4) \}$$
 (7)

while the mixed-integer convex constraints set of TN, denoted by  $\mathcal{X}_{v}$ , is defined as follows:

$$\mathcal{X}_{v} := \{(2a)-(2g), (2i), (2k)-(2n), (3), (5), (6)\}.$$
 (8)

# E. Coordinated dOPF-OTF Formulation Under the Decentralized Framework

This subsection presents the formulations of the coordinated dOPF-OTF problem under the decentralized framework. In our proposed framework, the power operator solves the following dOPF subproblem:

(PO.) 
$$\min_{\mathbf{x_p}, \alpha_p} f_p(\mathbf{x_p}) := \sum_i c_i^G p_i^G = \mathbf{c}^G \mathbf{p}^G$$
 (9a)

s.t. 
$$p^{\mathbf{D}} = z$$
 (9b)

$$x_{\mathbf{p}} \in \mathcal{X}_{\mathbf{p}}, \alpha_{\mathbf{p}} \in \{0, 1\},$$
 (9c)

where  $c^{G}$  is electricity price (can be interpreted as the transmission system's (grid) locational marginal prices (LMPs)) and  $p^{G}$  is electric power purchased by PDN from the grid. As such, the objective function (9a) minimizes the power purchased from the grid.  $p^{D}$  represents the power demand due to EVCSs in the dOPF model. Auxiliary variable z is utilized to facilitate the decentralized operation. All the decision variables of the PDN constraint set (7) are collectively referred to as  $x_{\rm p}$ while  $\alpha_{\rm p}$  collectively represents the integer decision variables. Even though there are no integer (including binary) variables present in the PDN constraint set (7), we have introduced binary variables  $\alpha_p$  in the compact form for the generalization (for the potential future adoption) of the proposed algorithm.

Similarly, the transportation coordinator solves the following OTF subproblem:

(TO.) 
$$\min_{\mathbf{x}_{\mathbf{v}}, \boldsymbol{\alpha}_{\mathbf{v}}} f_{\mathbf{v}}(\mathbf{x}_{\mathbf{v}}) := \sum_{rs} \sum_{q} f_{q}^{rs} C_{q}^{rs}$$
$$= \sum_{rs} F^{rs} C^{rs} = FC$$
(10a)
$$\text{s.t.} \quad \boldsymbol{p}^{\mathbf{T}} = \boldsymbol{z}$$
(10b)

s.t. 
$$p^{\mathrm{T}} = z$$
 (10b)

$$\mathbf{x}_{\mathbf{v}} \in \mathcal{X}_{\mathbf{v}}, \, \boldsymbol{\alpha}_{\mathbf{v}} \in \{0, 1\}, \tag{10c}$$

where  $x_v$  collectively represents all the decision variables while  $\alpha_v$  collectively represents the integer decision variables of the TN constraint set (8). And,  $p^{T}$  represents the power consumed by EVCSs in OTF. The objective function of the transportation subproblem (10a) minimizes the total cost of the transportation sector (i.e., time and energy consumption costs) [17]. Note that subscript **p** has been used for the dOPF symbols while v for the OTF symbols throughout the paper.

The decentralized formulation, i.e., (9) and (10) has one significant advantage: it does not require any entity with access to both  $\mathcal{X}_p$  and  $\mathcal{X}_v$ . It is important to note that there is no entity that has access to both PDN and TN information. Therefore, the proposed decentralized formulation of coordinated dOPF-OTF provides a practical framework that is compatible for the coordination of PDNs and TNs in the real world. Nonetheless, it can be observed from (9b) and (10b) that the two subproblems are still coupled through z as EVCS powers  $p^{T}$  in a TN act as a power demand  $p^{D}$  in a PDN. If two models are solved independently without being coordinated by a proper decentralized algorithm, the boundary variables, i.e.,  $p^{D}$  and  $p^{T}$  may not match with each other, which will result in increased cost or insecure operation of PDN. Therefore, in the next section, we introduce an enhanced SD-GS-AL decentralized algorithm that allows TNC and P-DSO to solve two subproblems separately but coordinately, with the guarantee of boundary variables matching.

#### III. THE PROPOSED ALGORITHM

This section first provides an overview of the proposed enhanced SD-GS-AL decentralized algorithm in Section III-A, describes the redesigned inner loop in the second subsection, and then proves the optimality and convergence in the third subsection.

# A. Overview of the Enhanced SD-GS-AL Algorithm

The key steps of the proposed enhanced SD-GS-AL algorithm are provided in Algorithm 1. The algorithm is initialized by assigning parameters in Step 1. Moreover, the starting points (i.e., for iteration 0) for the auxiliary variable z, binary variables  $\alpha_{\mathbf{p}}$  and  $\alpha_{\mathbf{v}}$ , Lagrangian multipliers  $\lambda_{\mathbf{p}}^{k}$  and  $\lambda_{\mathbf{v}}^{k}$ , and Lagrangian lower bounds  $\check{\phi}_p$  and  $\check{\phi}_v$  are assigned. Note that  $\alpha_{\rm p}$  and  $\alpha_{\rm v}$  collectively represent the binary variables of PDN and TN subproblems, respectively. For the initial values of auxiliary variable z and Lagrangian multipliers  $\lambda_{\mathbf{p}}^{k}$  and  $\lambda_{\mathbf{v}}^{k}$ , we can use zero. For the initial values of binary variables  $\alpha_{\rm p}$ and  $\alpha_v$ , we can use any feasible solution. For the Lagrangian lower bounds  $\check{\phi}_p$  and  $\check{\phi}_v$ , we can use any small negative number. Note that Step 2 to Step 8 constitutes the outer loop while (11) in Step 3 is the inner loop.

For any current iteration k, the first element of the Lagrangian relaxation value set  $LR^k$  is set to 0 while the difference of the Lagrangian relaxation value  $\Delta LR^k$  is initially set to a large number in Step 2. In addition, the initial values of auxiliary variable z, binary variables  $\alpha_p$  and  $\alpha_v$ , Lagrangian multipliers  $\lambda_{\mathbf{p}}^{k}$  and  $\lambda_{\mathbf{v}}^{k}$ , and Lagrangian lower bounds  $\check{\varphi}_{\mathbf{p}}$  and  $\check{\varphi}_{v}$  are set to that of the previous iteration k-1.

The  $L_{\gamma}^{p}$  in (11a) and  $L_{\gamma}^{v}$  in (11b) have the following detailed expressions in Step 3:

$$L_{\gamma}^{\mathbf{p}} := c^{\mathbf{G}} p^{\mathbf{G}} - (\lambda_{\mathbf{p}})^{\top} p^{\mathbf{D}} + \frac{\gamma}{2} \left\| z - p^{\mathbf{D}} \right\|_{2}^{2}, \tag{16a}$$

$$L_{\gamma}^{\mathbf{v}} := \mathbf{FC} + (\lambda_{\mathbf{v}})^{\top} \mathbf{p}^{\mathbf{T}} + \frac{\gamma}{2} \left\| \mathbf{p}^{\mathbf{T}} - \mathbf{z} \right\|_{2}^{2}.$$
 (16b)

Note that (16a) and (16b), the augmented Lagrangian relaxations of (9) and (10), respectively, are computed in parallel

## Algorithm 1 Enhanced SD-GS-AL Decentralized Algorithm

- 1: Parameters initialization:
  - 1) Parameters selection: Choose the outer loop convergence tolerance  $\epsilon$ , inner loop convergence tolerance  $\epsilon_u$ , penalty parameter  $\gamma$ , outer loop iteration limit K.
  - 2) Starting point: Starting points for auxiliary variable z, binary variables  $\alpha_p$  and  $\alpha_v,$  Lagrangian multipliers  $\lambda_p$  and  $\lambda_v,$  and Lagrangian lower bounds  $\check{\phi}_{D}$  and  $\check{\phi}_{V}$  are assigned by P-DSO and TNC, respectively.
- 2: Iteration initialization: Set LR<sup>k</sup>: = {0} and ΔLR<sup>k</sup>: = {a large number}, and {z, λ<sub>p</sub>, λ<sub>v</sub>, α<sub>p</sub>, α<sub>v</sub>, φ<sub>p</sub>, φ<sub>v</sub>}<sup>k</sup>: = {z, λ<sub>p</sub>, λ<sub>v</sub>, α<sub>p</sub>, α<sub>v</sub>, φ<sub>p</sub>, φ<sub>v</sub>}<sup>k-1</sup>.
  3: Lagrangian upper bound computation: While ΔLR<sup>k</sup> > ε<sub>u</sub>, repeat the
- following (11):

$$LR_{\mathbf{p}}^{k}, \mathbf{x_{\mathbf{p}}}^{k}, \mathbf{p^{D(k)}} \leftarrow \min_{\mathbf{x_{\mathbf{p}}, \mathbf{p^{D}}}} \left\{ L_{\gamma}^{\mathbf{p}} \left( \mathbf{x_{\mathbf{p}}, \mathbf{p^{D}}, z^{k}, \lambda_{\mathbf{p}}^{k}} \right) : \right.$$

$$\alpha_{\mathbf{p}} \in \alpha_{\mathbf{p}}^{k}, \mathbf{x_{\mathbf{p}}} \in \mathcal{X}_{\mathbf{p}} \right\}$$

$$LR_{\mathbf{v}}^{k}, \mathbf{x_{\mathbf{v}}}^{k}, \mathbf{p^{T(k)}} \leftarrow \min_{\mathbf{x_{\mathbf{v}}, \mathbf{p^{T}}}} \left\{ L_{\gamma}^{\mathbf{v}} \left( \mathbf{x_{\mathbf{v}}, \mathbf{p^{T}}, z^{k}, \lambda_{\mathbf{v}}^{k}} \right) : \right.$$

$$\left. (11a) \right.$$

$$\alpha_{\mathbf{v}} \in \alpha_{\mathbf{v}}^{k}, x_{\mathbf{v}} \in \mathcal{X}_{\mathbf{v}}$$
 (11b)

$$z^{k} \leftarrow \min_{z} \left\{ \left\| z - p^{\mathbf{D}(k)} \right\|_{2}^{2} + \left\| p^{\mathbf{T}(k)} - z \right\|_{2}^{2} \right\}$$
 (11c)

$$LR^k \leftarrow LR^k \cup \left\{ (LR_p^k + LR_v^k) \right\} \tag{11d}$$

$$\Delta LR^k \leftarrow LR^k_{end} - LR^k_{end-1} \tag{11e}$$

And, obtain the Lagrangian upper bounds as follows:

$$\hat{\varphi}_{\mathbf{p}}^{k} \leftarrow LR_{\mathbf{p}}^{k} + \frac{\gamma}{2} \left\| z^{k} - \mathbf{p}^{\mathbf{D}(k)} \right\|_{2}^{2} \tag{12a}$$

$$\hat{\varphi}_{\mathbf{v}}^{k} \leftarrow L R_{\mathbf{v}}^{k} + \frac{\gamma}{2} \left\| \boldsymbol{p}^{\mathbf{T}(k)} - \boldsymbol{z}^{k} \right\|_{2}^{2} \tag{12b}$$

- 4: Convergence check: If  $(\hat{\varphi}_p^k + \hat{\varphi}_v^k) (\check{\varphi}_p^k + \check{\varphi}_v^k) \le \epsilon$ , then terminate, and  $(x_{\mathbf{p}}^k, x_{\mathbf{v}}^k, z^k, \lambda_{\mathbf{p}}^k, \lambda_{\mathbf{v}}^k, \check{\varphi}_{\mathbf{p}}^k, \check{\varphi}_{\mathbf{v}}^k)$  is the solution. Otherwise, continue.
- 5: Lagrangian lower bound computation: Compute the intermediate Lagrangian lower bound as follows:

$$\tilde{\varphi}_{\mathbf{p}}, \alpha_{\mathbf{p}}^{k} \leftarrow \check{\varphi}_{\mathbf{p}} \left( \lambda_{\mathbf{p}}^{k} + \gamma \left( z^{k} - p^{\mathbf{D}(k)} \right) \right)$$
 (13a)

$$\tilde{\varphi}_{v}, \alpha_{v}^{k} \leftarrow \check{\varphi}_{v} \left( \lambda_{v}^{k} + \gamma \left( p^{\mathbf{T}(k)} - z^{k} \right) \right)$$
 (13b)

6: Lagrangian lower bound quality check: The intermediate Lagrangian lower bound passes the quality check, and iteration is declared forward iteration if the following inequality holds:

$$(\hat{\varphi}_{p}^{k} + \hat{\varphi}_{v}^{k}) \ge (\tilde{\varphi}_{p}^{k} + \tilde{\varphi}_{v}^{k}) \ge (\check{\varphi}_{p}^{k} + \check{\varphi}_{v}^{k}). \tag{14}$$

Perform the dual variables updates and keep the Lagrangian lower bounds if the iteration is declared forward:

$$\lambda_{\mathbf{p}}^{k} \leftarrow \lambda_{\mathbf{p}}^{k} + \gamma \left( z^{k} - \mathbf{p}^{\mathbf{D}(k)} \right)$$
 (15a)

$$\lambda_{\mathbf{v}}^{k} \leftarrow \lambda_{\mathbf{v}}^{k} + \gamma \left( p^{\mathbf{T}(k)} - z^{k} \right)$$
 (15b)

$$\check{\varphi}_{\mathrm{p}}^{k} \leftarrow \tilde{\varphi}_{\mathrm{p}}^{k} \tag{15c}$$

$$\check{\varphi}_{\mathbf{v}}^{k} \leftarrow \tilde{\varphi}_{\mathbf{v}}^{k} \tag{15d}$$

Otherwise, the iteration is declared neutral: Algorithm continues without

7: **Loop:** Set k = k + 1 and go back to Step 2.

by P-DSO and TNC, respectively. Moreover,  $LR_p^k$  and  $LR_v^k$ represent the values of Lagrangian relaxations (16a) and (16b), respectively. In (16a) and (16b), binary variables are fixed so that PDN and TN sub-problems are continuous. The binary variables are fixed from the solutions of the previous iteration of MIP subproblems in Step 5. Moreover, the auxiliary variable z is computed as in (11c). The auxiliary variable update (11c)

can be assigned to either of the operators (in our study, we assign it to the TN coordinator) as the only information shared is the boundary variables from both networks. Moreover, the Lagrangian relaxation value set  $LR^k$  is updated as in (11d) while the difference of the Lagrangian relaxation value  $\Delta LR^k$ is updated as in (11e), where the two most recent elements of  $LR^k$  are utilized (subscript *end* represents the most recent element). Finally, the Lagrangian upper bounds  $\hat{\varphi}_{p}$  and  $\hat{\varphi}_{v}$ are computed as in (12) in Step 3. Note that Algorithm 1 is said to converge if the difference of Lagrangian bounds  $(\hat{\varphi}_p + \hat{\varphi}_v) - (\check{\varphi}_p + \check{\varphi}_v))$  is within the limit of tolerance, as stated in Step 4. In this paper, the proposed enhanced SD-GS-AL algorithm is used to coordinate the MICP subproblems. Therefore, it converges to the global optimal solution of the centralized implementation of MICP subproblems.

The  $\check{\phi}_p$  and  $\check{\phi}_v$  ((13a) and (13b) respectively), which are used to obtain the intermediate Lagrangian lower bounds  $\tilde{\varphi}_{\rm p}$ and  $\tilde{\varphi}_{v}$  and to update binary variables  $\alpha_{p}$  and  $\alpha_{v}$  in Step 5, are computed in parallel by P-DSO and TNC, respectively, and are given as follows:

$$\check{\varphi}_{\mathbf{p}}(\lambda_{\mathbf{p}}^{k}) := \min_{x_{\mathbf{p}}, p^{\mathbf{D}}, \alpha_{\mathbf{p}}} \left\{ c^{\mathbf{G}} p^{\mathbf{G}} - (\lambda_{\mathbf{p}}^{k})^{\top} p^{\mathbf{D}} : x_{\mathbf{p}} \in \mathcal{X}_{\mathbf{p}} \right\}, \quad (17a)$$

$$\check{\varphi}_{\mathbf{v}}\left(\boldsymbol{\lambda}_{\mathbf{v}}^{k}\right) := \min_{\boldsymbol{x}_{\mathbf{v}}, \boldsymbol{p}^{\mathbf{T}}, \boldsymbol{\alpha}_{\mathbf{v}}} \left\{ \boldsymbol{F}\boldsymbol{C} + (\boldsymbol{\lambda}_{\mathbf{v}}^{k})^{\top} \boldsymbol{p}^{\mathbf{T}} : \boldsymbol{x}_{\mathbf{v}} \in \mathcal{X}_{\mathbf{v}} \right\}. \tag{17b}$$

Note that no variables (including binary) are fixed in Step 5, although binary variables are fixed in Step 3. The intermediate Lagrangian lower bounds  $(\check{\phi}_p \text{ and } \check{\phi}_v)$  computed in Step 5 go through a quality check in Step 6. If the intermediate Lagrangian lower bounds calculated in Step 5 are greater than the previously calculated lower bounds  $(\check{\varphi}_{p}^{k})$  and  $\check{\varphi}_{v}^{k}$ and smaller than the current upper bounds  $(\hat{\varphi}_{p}^{k} \text{ and } \hat{\varphi}_{v}^{k})$  as stipulated in (14), the intermediate lower bounds pass the quality check (iteration is declared forward), and Lagrangian multipliers are updated in a decentralized manner as in (15a) and (15b). Moreover, the Lagrangian lower bounds ( $\check{\phi}_{\rm p}^k$  and  $\check{\phi}_{v}^{k}$ ) are also updated as in (15c) and (15d). Otherwise, the algorithm continues without updates. It is worth noting that all the computations, including lagrangian multipliers update, are performed in Algorithm 1 by P-DSO and TNC in parallel.

Note that the proposed algorithm requires setting four parameters: outer loop convergence tolerance  $(\epsilon)$ , inner loop convergence tolerance  $(\epsilon_{ij})$ , penalty parameter  $(\gamma)$ , and outer loop iteration limit (K). While most of these parameters are standard in augmented Lagrangian-based algorithms [37], the penalty parameter  $(\gamma)$  is pivotal in determining the step size in any augmented Lagrangian-based algorithm. If the penalty parameter  $(\gamma)$  is set too small, the algorithm could take a long time to converge. If it is set too high, it could overstep the optimal point, and the algorithm may not converge. Thus, erring toward a smaller  $\gamma$  is advisable to ensure systematic progress toward the optimal solution in accordance with standard augmented Lagrangian penalty parameter guidelines.

# B. Why Does the Enhanced SD-GS-AL Algorithm Outperform the Original One?

In the SD-GS-AL algorithms, the purpose of the inner loop is to compute the optimal value of Lagrangian relaxation of Authorized licensed use limited to: University of Central Florida. Downloaded on December 24,2024 at 00:26:28 UTC from IEEE Xplore. Restrictions apply.

subproblems for a given value of Lagrangian multipliers. The original SD-GS-AL algorithm [31] defines the inner loop as follows:

Repeat (18)  $t_{max}$  times:

$$LR_{\mathbf{p}}^{k}, \mathbf{x_{\mathbf{p}}}^{k}, \mathbf{p^{D(k)}} \leftarrow \min_{\mathbf{x_{\mathbf{p}}, \mathbf{p^{D}}}} \left\{ L_{\gamma}^{\mathbf{p}} \left( \mathbf{x_{\mathbf{p}}, \mathbf{p^{D}}}, \mathbf{z^{k}}, \lambda_{\mathbf{p}}^{k} \right) : \right.$$

$$\left. \alpha_{\mathbf{p}} \in \alpha_{\mathbf{p}}^{k}, \mathbf{x_{\mathbf{p}}} \in \mathcal{X}_{\mathbf{p}} \right\}$$

$$\left. \left( 18a \right) \right.$$

$$LR_{\mathbf{v}}^{k}, \mathbf{x_{\mathbf{v}}}^{k}, \mathbf{p^{T(k)}} \leftarrow \min_{\mathbf{x_{\mathbf{v}}, \mathbf{p^{T}}}} \left\{ L_{\gamma}^{\mathbf{v}} \left( \mathbf{x_{\mathbf{v}}, \mathbf{p^{T}}, z^{k}, \lambda_{\mathbf{v}}^{k}} \right) : \right\}$$

$$\alpha_{\mathbf{v}} \in \alpha_{\mathbf{v}}^{k}, x_{\mathbf{v}} \in \mathcal{X}_{\mathbf{v}}$$
 (18b)

$$\boldsymbol{z}^{k} \leftarrow \min_{\boldsymbol{z}} \left\{ \left\| \boldsymbol{z} - \boldsymbol{p}^{\mathbf{D}(k)} \right\|_{2}^{2} + \left\| \boldsymbol{p}^{\mathbf{T}(k)} - \boldsymbol{z} \right\|_{2}^{2} \right\}, \tag{18c}$$

where  $t_{max}$  is the pre-defined number of inner loop iterations. However, there is a critical issue associated with such a setting. Namely, for a specific problem, a proper value of  $t_{max}$  is unknown in advance. If  $t_{max}$  is too small, the algorithm may not converge as the calculated value of Lagrangian relaxation may not be optimal. If  $t_{max}$  is too big, the algorithm takes a long time to converge.

To avoid this issue, we propose a new inner loop as given in (11), yielding an enhanced SD-GS-AL algorithm. In (11), we designed a stopping criterion using which the algorithm judges whether to stop the inner loop. To be specific, the current value of Lagrangian relaxation is checked for convergence before each new inner loop iteration. If the difference between current and previous values of Lagrangian relaxation (denoted by  $\Delta LR^k$ ) is within the limit of the inner loop convergence tolerance (denoted by  $\epsilon_u$ ), the new inner loop iteration is not executed. On the other hand, if the difference exceeds the tolerance, the inner loop proceeds with a new iteration, employing the most recent parameter and variable values as specified in Step 3.

As such, the new algorithm no longer relies on the pre-determined  $t_{max}$  and can automatically and intelligently determine when to stop the inner loop for each outer loop iteration. It brings two advantages. First, it prevents the inner loop from continuing unnecessarily after the Lagrangian value has already converged after a few iterations, thereby saving time and computational resources. Second, it helps prevent the convergence failures of the original algorithm, which are caused by setting too small  $t_{max}$ .

# C. Optimality and Convergence

In [31], the original SD-GS-AL algorithm has been proved for convergence and optimality. Nonetheless, the inner loop has been redesigned in the proposed enhanced SD-GS-AL algorithm. In this subsection, we will prove that convergence and optimality still hold under the new inner loop.

**Theorem:** The sequence  $\{(x^k, z^k)\}$  generated by the Algorithm 1 converges to the global optimal solution of MICP dOPF and OTF subproblems as  $k \to \infty$ .

**Proof:** We introduce the following definitions for brevity and conciseness:

$$L := L_{\nu}^{p} + L_{\nu}^{v}, \tag{19a}$$

$$\varphi^{c}(\lambda) := \varphi_{p}^{c}(\lambda_{p}) + \varphi_{v}^{c}(\lambda_{v}), \tag{19b}$$

$$\varphi_{\mathbf{p}}^{\mathbf{c}}(\mathbf{\lambda}_{\mathbf{p}}^{k}) := \min_{\mathbf{x}_{\mathbf{p}}, \mathbf{p}^{\mathbf{D}}} \left\{ c^{\mathbf{G}} \mathbf{p}^{\mathbf{G}} - (\mathbf{\lambda}_{\mathbf{p}}^{k})^{\top} \mathbf{p}^{\mathbf{D}} : \mathbf{x}_{\mathbf{p}} \in \mathrm{CH}(\mathcal{X}_{\mathbf{p}}) \right\}, (19c)$$

$$\varphi_{\mathbf{v}}^{\mathbf{c}}(\mathbf{\lambda}_{\mathbf{v}}^{k}) := \min_{\mathbf{x}_{\mathbf{v}}, \mathbf{p}^{\mathbf{T}}} \left\{ \mathbf{FC} + (\mathbf{\lambda}_{\mathbf{v}}^{k})^{\top} \mathbf{p}^{\mathbf{T}} : \mathbf{x}_{\mathbf{v}} \in \mathrm{CH}(\mathcal{X}_{\mathbf{v}}) \right\}, \quad (19d)$$

$$CH(.) := Convex Hulls,$$
 (19e)

$$\check{\varphi}(\lambda) := \check{\varphi}_{\mathbf{p}}(\lambda_{\mathbf{p}}) + \check{\varphi}_{\mathbf{v}}(\lambda_{\mathbf{v}}), \tag{19f}$$

$$\hat{\varphi}(\mathbf{x}, \mathbf{z}, \lambda) := \hat{\varphi}_{\mathbf{p}}(\mathbf{x}_{\mathbf{p}}, \mathbf{z}, \lambda_{\mathbf{p}}) + \hat{\varphi}_{\mathbf{v}}(\mathbf{x}_{\mathbf{v}}, \mathbf{z}, \lambda_{\mathbf{v}}), \tag{19g}$$

$$\mathcal{X} \coloneqq \mathcal{X}_{p} \cup \mathcal{X}_{v},\tag{19h}$$

$$\mathbf{x}^k := (\mathbf{x_n}^k, \mathbf{x_v}^k)$$
 (vector concatenation), (19i)

$$(x-z) := \left( \left( p^{\mathbf{T}} - z \right), \left( z - p^{\mathbf{D}} \right) \right). \tag{19j}$$

The convergence condition at  $x \in \mathcal{X}$  for a limit point  $(\bar{x}, \bar{z})$  of the sequence  $\{(x^k, z^k)\}$  is defined as [31]:

$$L_{\mathbf{x}}'(\mathbf{x}, \mathbf{z}; s) \ge 0 \quad \text{for all } s \in \mathcal{X} - \{\mathbf{x}\},$$
 (20)

where  $L_x'(x,z;s) = \lim_{\beta \to 0} \frac{L(x+\beta s,z)-L(x,z)}{\beta}$  for some  $\beta$ . The Direction Related Assumption is given as follows: for

The Direction Related Assumption is given as follows: for any iteration k,  $s^k$  is chosen such that  $x^k + s^k \in \mathcal{X}$  and  $L'_{\mathbf{r}}(x, z; s) \geq 0$ . Note that  $s^k$  is a gradient of  $x^k$ .

The proof has three parts. Part 1 proves the convergence of the proposed algorithm, Part 2 verifies the optimality, and Part 3 provides convergence of the boundary variables.

Part 1: The sequence  $\{(\mathbf{x}^k, \mathbf{z}^k)\}$  generated by Step 3 in Algorithm 1 always converges to the limit point  $(\bar{\mathbf{x}}, \bar{\mathbf{z}})$ .

Here, we prove that the limit point  $(\bar{x}, \bar{z})$  of the sequence  $\{(x^k, z^k)\}$  of feasible solutions to the problems (9) and (10) satisfies the convergence condition (20). Note that subproblems in Step 3 are continuous as integer variables are fixed. According to the Armijo rule, we have

$$\frac{L(\mathbf{x}^k + \beta^k s^k, \mathbf{z}^k) - L(\mathbf{x}^k, \mathbf{z}^k)}{\beta^k} \le \sigma L_{\mathbf{x}}'(\mathbf{x}^k, \mathbf{z}^k; s^k)$$
 (21)

for any  $\sigma \in (0,1)$ . Note that  $\beta^k$  is the step length of the Armijo rule. As  $L_{\mathbf{x}}'(\mathbf{x}^k, \mathbf{z}^k; \mathbf{s}^k) < 0$  according to the Direction Related Assumption (defined above) and  $\beta^k \geq 0$ , above expression can be rewritten as  $L(\mathbf{x}^k + \beta^k \mathbf{s}^k, \mathbf{z}^k) < L(\mathbf{x}^k, \mathbf{z}^k)$ . We also have  $L(\mathbf{x}^{k+1}, \mathbf{z}^{k+1}) \leq L(\mathbf{x}^k + \beta^k \mathbf{s}^k, \mathbf{z}^k) < L(\mathbf{x}^k, \mathbf{z}^k)$  and  $L(\mathbf{x}^{k+1}, \mathbf{z}^{k+1}) < L(\mathbf{x}^k, \mathbf{z}^k)$ . Also, L is bounded from below, we have  $\lim_{k \to \infty} L(\mathbf{x}^k, \mathbf{z}^k) = \bar{L} > -\infty$ . Hence, we have

$$\lim_{k\to\infty} L(\mathbf{x}^{k+1}, \mathbf{z}^{k+1}) - L(\mathbf{x}^k, \mathbf{z}^k) = 0.$$

Furthermore

$$\lim_{k \to \infty} L\left(x^k + \beta^k s^k, z^k\right) - L\left(x^k, z^k\right) = 0. \tag{22}$$

For the sake of contradiction, we assume that  $\lim_{k\to\infty}(x^k,z^k)=(\bar x,\bar z)$  does not satisfy the convergence condition (20). From the definition of gradient-related assumption, we have

$$\limsup_{k \to \infty} L_x'\left(\mathbf{x}^k, \mathbf{z}^k; s^k\right) < 0. \tag{23}$$

Hence, in conclusion,  $\lim_{k\to\infty} \beta^k = 0$ . From Armijo rule, after a certain iteration  $k \geq \bar{k}$ , we can define  $\{\bar{\beta}^k\}$ ,  $\bar{\beta}^k = \beta^k/\gamma$  for some  $\gamma$ , where  $\bar{\beta}^k \leq 1$  and we have

$$\sigma L_{\mathbf{x}}'\left(\mathbf{x}^{k}, \mathbf{z}^{k}; s^{k}\right) < \frac{L\left(\mathbf{x}^{k} + \bar{\beta}^{k} s^{k}, \mathbf{z}^{k}\right) - L\left(\mathbf{x}^{k}, \mathbf{z}^{k}\right)}{\bar{\beta}^{k}}.$$
 (24)

If we apply the mean value theorem to the right side of the above expression, for some  $\tilde{\beta}^k \in [0, \bar{\beta}^k]$ , we have

$$\sigma L_{\mathbf{x}}'\left(\mathbf{x}^{k}, \mathbf{z}^{k}; s^{k}\right) < L_{\mathbf{x}}'\left(\mathbf{x}^{k} + \widetilde{\beta}^{k} s^{k}, \mathbf{z}^{k}; s^{k}\right). \tag{25}$$

Moreover,  $\limsup_{k\to\infty} L_x'(x^k,z^k;s^k) < 0$ , and if we take a limit point  $\bar{s}$  of  $\{s^k\}$  such that  $L_x'(\bar{x},\bar{z},\bar{s}) < 0$ . Also, we have,  $\lim_{k\to\infty,k\in\mathcal{K}} L_x'(x^k,z^k;s^k) = L_x'(\bar{x},\bar{z};\bar{s})$  and  $\lim_{k\to\infty,k\in\mathcal{K}} L_x'(x^k+\widetilde{\beta}^ks^k,z^k;s^k) = L_x'(\bar{x},\bar{z};\bar{s})$ . From these two factors, we can infer that  $L_x'(x,z;s)$  is continuous. Now, from expression (25), we have

$$\sigma L_{\mathbf{r}}'(\bar{\mathbf{x}},\bar{\mathbf{z}};\bar{s}) \leq L_{\mathbf{r}}'(\bar{\mathbf{x}},\bar{\mathbf{z}};\bar{s}) \quad \Longrightarrow \quad 0 \leq (1-\sigma)L_{\mathbf{r}}'(\bar{\mathbf{x}},\bar{\mathbf{z}};\bar{s}).$$

Since  $(1-\sigma)>0$ ,  $L_x'(\bar{x},\bar{z};\bar{s})<0$  which is a contradiction. Therefore, the limit point  $(\bar{x},\bar{z})$  of the sequence  $\{(x^k,z^k)\}$  i.e.,  $\lim_{k\to\infty}(x^k,z^k)=(\bar{x},\bar{z})$  satisfies the convergence condition, which means Step 3 in Algorithm 1 has a limit point. It is worth noting that the solution of Step 3 is reported as the final solution when the algorithm converges, as stated in Step 4; this part of the proof shows that Algorithm 1 has a converged solution.

Part 2: The limit point  $(\bar{x}, \bar{z})$  of the sequence  $\{(x^k, z^k)\}$  generated by Step 3 in Algorithm 1 is a global optimal solution of the MICP subproblems.

From *Part 1*, we have that the algorithm converges to the limit point  $(\bar{x}, \bar{z})$ . In other words, the algorithm produces a solution,  $(\bar{x}, \bar{z})$ . Here, we establish the global optimality of the solution  $(\bar{x}, \bar{z})$ . The optimality conditions (KKT conditions) associated with the  $(\bar{x}, \bar{z}) \in \operatorname{argmin}_{x,z}\{L(x, z, \lambda): \alpha \in \alpha^k\}$  is given as follows:

$$\Phi_{\mathbf{x}} := \left[ \nabla f(\bar{\mathbf{x}}) + [\lambda + \gamma(\bar{\mathbf{x}} - \bar{\mathbf{z}})]^{\mathsf{T}} \mathbf{1} \right]^{\mathsf{T}} \left[ \mathbf{x} - \bar{\mathbf{x}} \right]$$
> 0.

Note that integer (binary) variables are fixed here. The above optimality condition can also be written as:

$$\min_{x} \{\Phi_x\} = 0.$$

The above expression can be re-written in terms of  $\check{\phi}(\lambda + \gamma(\bar{x} - \bar{z}), \bar{x})$  as:

$$\check{\varphi}(\lambda + \gamma(\bar{x} - \bar{z}), \bar{x}) = f(\bar{x}) + \lambda^{\top} \bar{x} + \gamma \|\bar{x} - \bar{z}\|_{2}^{2}$$

$$= L(\bar{x}, \bar{z}, \lambda) + \frac{\gamma}{2} \|\bar{x} - \bar{z}\|_{2}^{2}.$$

We have,

$$\check{\varphi}(\lambda, x^k) := \min_{\mathbf{x}} \Big\{ f(x^k) + \nabla_{\mathbf{x}} f(x^k)^\top (\mathbf{x} - x^k) \\
+ \lambda^\top x : \mathbf{x} \in \mathcal{X} \Big\}.$$

Note that according to [38], minimizing linear objective function over mixed-integer convex sets  $\mathcal{X}_p$  and  $\mathcal{X}_v$  is equivalent

to minimizing linear objective function over convex hulls sets,  $CH(\mathcal{X}_p)$  and  $CH(\mathcal{X}_v)$ . Also, we have

$$\hat{\varphi}(\bar{x},\bar{z},\lambda) := L(\bar{x},\bar{z},\lambda) + \frac{\gamma}{2} \|\bar{x} - \bar{z}\|_2^2.$$

Hence for a unique solution,

$$\check{\varphi}(\lambda + \gamma(\bar{x} - \bar{z}), \bar{x}) = \hat{\varphi}(\bar{x}, \bar{z}, \lambda) = \varphi^{c}(\bar{x}, \bar{z}, \lambda). \tag{26}$$

The expression (26) implies that the upper and lower bounds of the Lagrangian function converge as  $k \to \infty$ . In other words, Algorithm 1 converges to the global optimal solution of the centralized implementation of MICP subproblems.

Part 3: The boundary variables ( $p^D$  and  $p^T$ ) also match when the Lagrangian upper and lower bounds match as  $k \to \infty$ .

In *Part* 2, we have shown that the upper and lower bounds of Lagrangian match as  $k \to \infty$ . In this part, we show that the boundary variables  $(p^D \text{ and } p^T)$  also match as  $k \to \infty$ . From (11a), (11b), (12), and (16), the Lagrangian upper bound is given as follows,

$$\hat{\varphi} = \hat{\varphi}_{p} + \hat{\varphi}_{v}$$

$$= c^{G} p^{G} - (\lambda_{p})^{T} p^{D} + \gamma \left\| z - p^{D} \right\|_{2}^{2}$$

$$+ FC + (\lambda_{v})^{T} p^{T} + \gamma \left\| p^{T} - z \right\|_{2}^{2}. \tag{27}$$

From (17), the Lagrangian lower bound is given as follows,

$$\dot{\varphi} = \dot{\varphi}_{p} + \dot{\varphi}_{v} 
= c^{G} p^{G} - (\lambda_{p})^{T} p^{D} + FC + (\lambda_{v})^{T} p^{T}.$$
(28)

From *Part 2*, we have that  $\hat{\varphi} = \check{\varphi} \Rightarrow \hat{\varphi} - \check{\varphi} = 0$  as  $k \to \infty$ . This can be expressed in terms of (27) and (28) as follows,

$$\gamma \left\| z - \boldsymbol{p}^{\mathbf{D}} \right\|_{2}^{2} + \gamma \left\| \boldsymbol{p}^{\mathbf{T}} - z \right\|_{2}^{2} = 0. \tag{29}$$

For positive values of  $\gamma$ ,  $p^{D}$ ,  $p^{T}$ , and z, the followings must hold to make left side of (29) equal the right side of (29),

$$z - p^{\mathbf{D}} = 0$$

$$p^{\mathbf{T}} - z = 0$$
i.e., 
$$p^{\mathbf{D}} = p^{\mathbf{T}}.$$
(30)

The expression (30) represents that the boundary variables ( $p^{\mathbf{D}}$  and  $p^{\mathbf{T}}$ ) match when the Lagrangian upper and lower bounds match as  $k \to \infty$ .

#### IV. CASE STUDY

We tested the proposed enhanced SD-GS-AL algorithm on three power-transportation systems. In this section, the simulation setup is first described. Second, the advantages of the proposed method are illustrated via simulation results.

#### A. Simulation Setup

Generally, the covered area of TN is much larger than that of a power distribution feeder. Therefore, to make the area of coverage similar, one power distribution feeder supplies one EVCS in a TN in this paper, as in [33]. For Case 1, the three modified IEEE 13-node test feeders represent the PDN, while

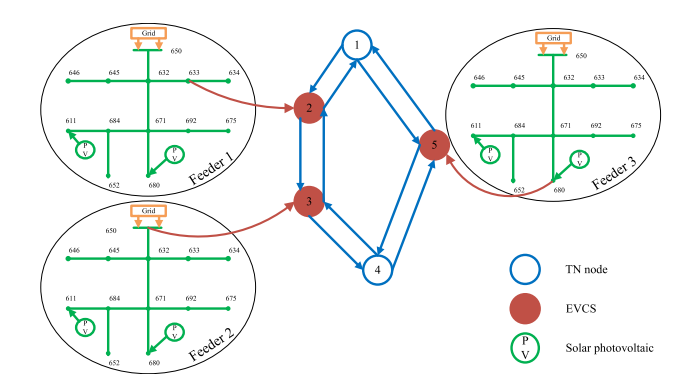


Fig. 2. PDN and TN topology (Case 1).

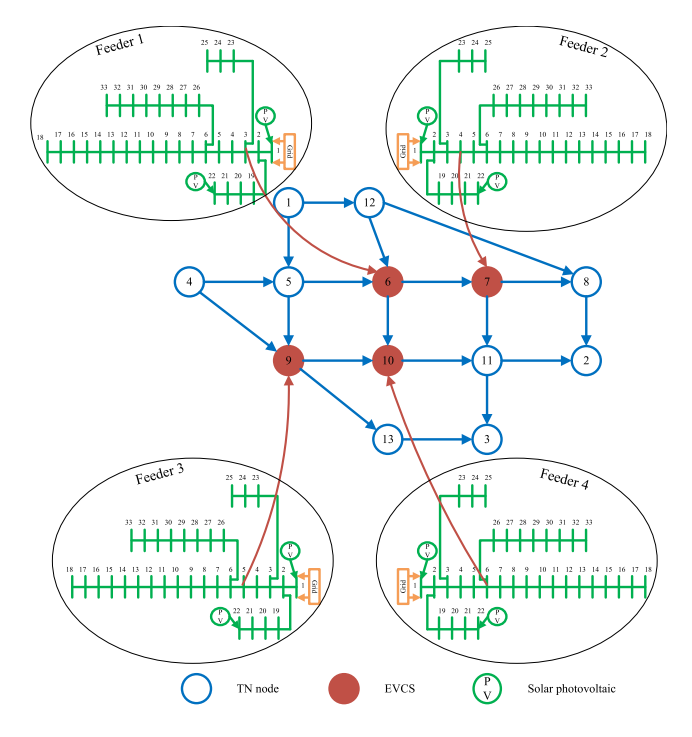


Fig. 3. PDN and TN topology (Case 2).

the 5-node road network represents the TN, as shown in Fig. 2. For Case 2, the four modified IEEE 33-node test feeders are used to represent the PDN, while the modified Nguyen-Dupius network is adopted to represent the TN, as shown in Fig. 3. For Case 3, the four modified IEEE 123-node test feeders are used to represent the PDN, while the modified Sioux Falls network [39] is adopted to represent the TN, as shown in Fig. 4. It is worth mentioning that feeders are not coupled with each other, and they are supplied by different buses of the transmission network (grid), hence different grid prices (can be interpreted as LMPs of transmission system). The details of the physical coupling between TN and PDN and the grid prices used are provided in Table I. In Figures 2 and 3, the network drawn in green color represents the feeder, while the network drawn in blue color represents TN. For Case 3, shown in Figure 4, the feeder topology is not drawn for brevity.

The arcs parameters for TN of Case 1 are provided in Table II, while those of Case 2 and 3 are adopted from [13] and [39], respectively. For Case 1, two O-D pairs considered

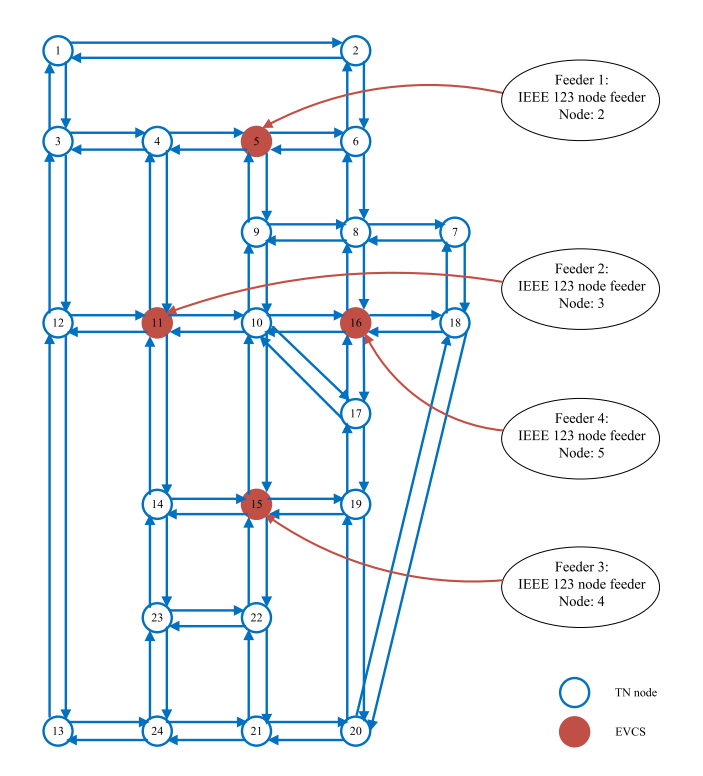


Fig. 4. PDN and TN topology (Case 3).

TABLE I Information on the Physical Coupling Between TN and PDN and Grid Prices

		Feeder 1	Feeder 2	Feeder 3	Feeder 4
	TN Node	2	3	5	
Case 1	Feeder Node	633	650	680	
	Grid Price (\$/MWh)	70.47	77.52	84.57	
	TN Node	6	7	9	10
Case 2	Feeder Node	3	4	5	6
	Grid Price (\$/MWh)	70.47	77.52	84.57	91.62
	TN Node	5	11	16	15
Case 3	Feeder Node	2	3	4	5
	Grid Price (\$/MWh)	70.47	77.52	84.57	91.62

TABLE II
TN ARCS PARAMETERS (CASE 1)

art End $t_a^0$		$c_a$	$d_a$
	(min.)	(per min.)	(miles)
2/1	120	40	150
3/2	130	40	150
4/3	120	40	150
4/1	195	47	225
5/4	195	47	225
	2/1 3/2 4/3 4/1	2/1 120 3/2 130 4/3 120 4/1 195	(min.)         (per min.)           2/1         120         40           3/2         130         40           4/3         120         40           4/1         195         47

are  $1\rightarrow 4$  and  $4\rightarrow 1$  with a traffic (EV) demand of 30 each. For Case 2, four O-D pairs considered are  $1\rightarrow 2$ ,  $1\rightarrow 3$ ,  $4\rightarrow 2$ , and  $4\rightarrow 3$  with a traffic demand of 60 each. For Case 3, six O-D pairs considered are  $1\rightarrow 20$ ,  $2\rightarrow 13$ ,  $3\rightarrow 19$ ,  $4\rightarrow 18$ ,  $12\rightarrow 7$ , and  $23\rightarrow 6$  with a traffic demand of 60 each. The capacity of each solar photovoltaic (PV) used in the feeders of all cases is 200 KW. While the locations of PVs of the first two test cases are shown in Figures 2 and 3, the locations

TABLE III
ALGORITHM PARAMETERS

	$\epsilon/\epsilon_u$	$\gamma$	K	$\boldsymbol{z}^0$	$oldsymbol{\lambda}_{\mathbf{p}}^0 ackslash oldsymbol{\lambda}_{\mathbf{v}}^0$	$\check{arphi}^0_{ m p}$	$\check{arphi}_{ m v}^0$
Case 1	6e-3/1e-1	4e-6	300	0	0	-9999	-99999
Case 2	6e-3/1e-1	4e-6	200	0	0	-9999	-99999
Case 3	6e-3/2e-1	4e-6	200	0	0	-9999	-99999

of PVs in the feeders of Case 3 are nodes–19, 47, and 76. Moreover, the parameters used for the proposed algorithm are provided in Table III.

It should be noted that in the TN model, all feasible paths for each origin-destination pair can be used as input. However, in a larger network, the number of feasible paths can become overwhelming. Additionally, not all feasible paths for a given origin-destination pair are actually used by electric vehicles, as many of them are much longer and thus more costly than shorter alternatives. To address this issue, we have narrowed down the set of feasible paths by following a specific rule. First, all paths for each origin-destination pair are generated. Then, any paths that do not contain at least one EVCS node are removed as infeasible. Finally, any feasible paths that are longer than twice the length of the shortest path (in terms of distance) are also removed.

#### B. Validation of the Proposed Algorithm

In this subsection, the proposed enhanced SD-GS-AL algorithm is validated and compared with the original SD-GS-AL algorithm [31] and ADMM [40] using three test cases.

1) Case-1: IEEE 13-Node PDN and 5-Node TN: This subsection exhibits the results of the coordination of TN and PDN through numerical experiments on a test system, shown in Figure 2. The proposed algorithm is compared with the ADMM and the original SD-GS-AL. Since the difference of Lagrangian upper and lower bounds (also called convergence error) is used as a convergence criterion in the proposed and original SD-GS-AL algorithms, and the difference of boundary variables is used as a convergence criterion in the ADMM [40], two types of plots are utilized for unit consistency in the comparison. First, the plot of convergence error (i.e., the difference of Lagrangian bounds) is compared for both the proposed and original SD-GS-AL algorithms, as shown in Figure 5. Note that the ADMM does not utilize the concept of Lagrangian bounds; therefore, it is not included in Figure 5. Second, the plot of boundary error (i.e., the sum of the absolute difference of all boundary variables) has been utilized for comparison with ADMM, as shown in Figure 6. The figures illustrate that the proposed enhanced SD-GS-AL algorithm outperforms ADMM and original SD-GS-AL as they failed to converge after 300 outer iterations. Note that a non-zero error indicates the original SD-GS-AL algorithm and ADMM failed to converge. The convergence and boundary errors of only 20 iterations are shown in Figures 5 and 6 for better visualization.

2) Case-2: IEEE 33-Node PDN and Modified Nguyen-Dupius TN: This subsection provides the results of the coordination of TN and PDN through numerical experiments

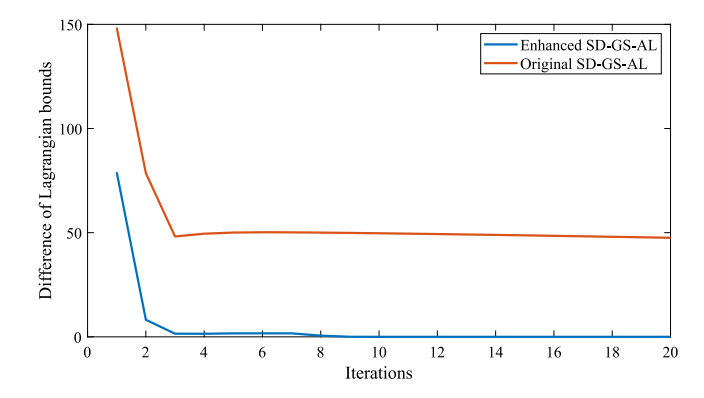


Fig. 5. Comparison of the convergence error (i.e., the difference of Lagrangian bounds) of the proposed enhanced SD-GS-AL algorithm and the original SD-GS-AL algorithm (with one inner loop iteration) (Case 1).

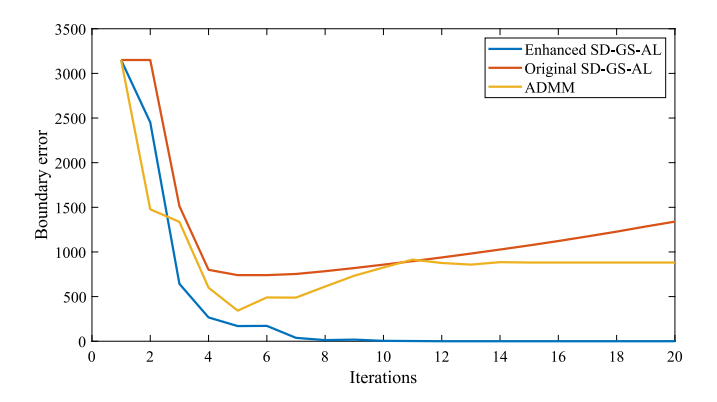


Fig. 6. Comparison of the boundary error (i.e., the difference of boundary variables) of the proposed enhanced SD-GS-AL algorithm, the original SD-GS-AL algorithm (with one inner loop iteration), and the ADMM (Case 1).

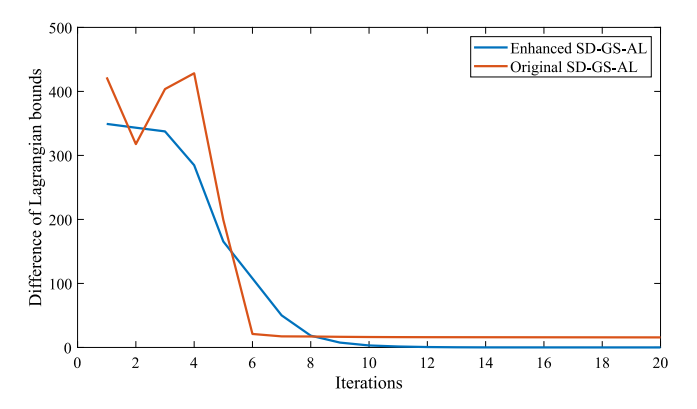


Fig. 7. Comparison of the convergence error (i.e., the difference of Lagrangian bounds) of the proposed enhanced SD-GS-AL algorithm and the original SD-GS-AL algorithm (with one inner loop iteration) (Case 2).

on a bigger system. The topology of the transportation network and the power distribution feeder is shown in Fig. 3. As in Case 1, the proposed algorithm is compared with the ADMM and the original SD-GS-AL [31] as presented in Figures 7 and 8. The figures illustrate that the proposed enhanced SD-GS-AL algorithm outperforms ADMM and original SD-GS-AL as they failed to converge after 200 outer iterations. For better visualization, the errors of only 20 iterations are shown in Figure 7 and 8.

	Algorithm	Number of inner	Total inner	Total outer	Converged?	Objective	Computational
		loop iterations	loop iterations	loop iterations	e o iii e i ge u i	value	time
	Enhanced SD-GS-AL	N/A	28	10	Yes	\$29941.16	101.1 s
Case 1	Original SD-GS-AL	1	300	300	No	N/A	N/A
Case 1	Original 3D-03-AL	8	104	13	Yes	\$29941.11	243.1 s
	ADMM	N/A	N/A	300	No	N/A	N/A
	Centralized	N/A	N/A	N/A	Yes	\$29941.21	11.2 s
	Enhanced SD-GS-AL	N/A	56	20	Yes	\$ 49549.04	200.4 s
Case 2	Original SD-GS-AL	1	200	200	No	N/A	N/A
Case 2	Original 3D-03-AL	5	110	22	Yes	\$ 49549.02	342.9 s
	ADMM	N/A	N/A	200	No	N/A	N/A
	Centralized	N/A	N/A	N/A	Yes	\$ 49549.13	19.2 s
	Enhanced SD-GS-AL	N/A	80	32	Yes	\$ 59218.29	440 s
Case 3	Original SD-GS-AL	1	200	200	No	N/A	N/A
Case 3	Oliginal 3D-03-AL	12	468	39	Yes	\$ 59218.30	1092 s
	ADMM	N/A	N/A	200	No	N/A	N/A
	Centralized	N/A	N/A	N/A	Yes	\$ 59218.35	30.2 s

TABLE IV
COMPARISON OF COMPUTATIONAL PERFORMANCE

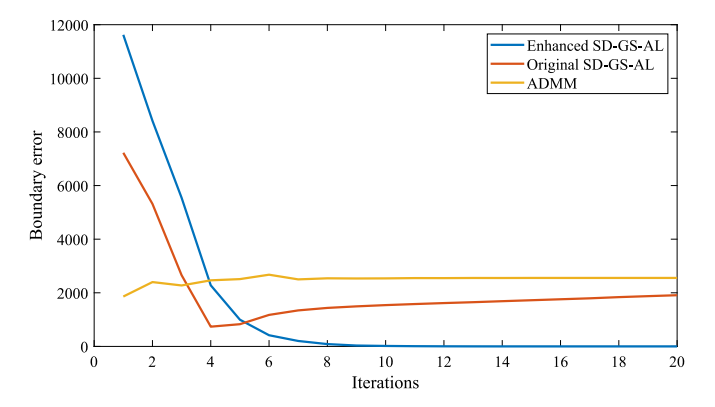
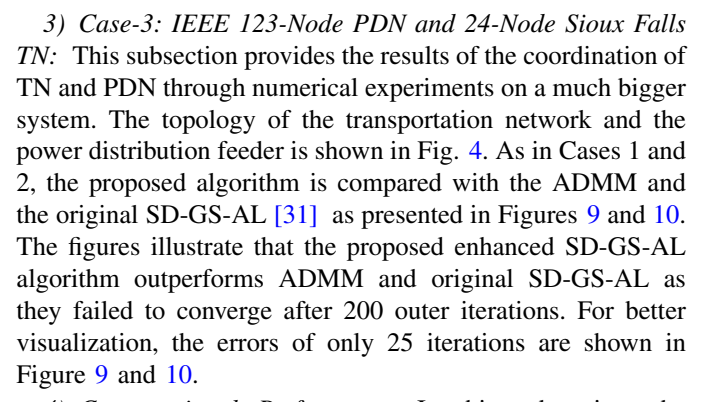
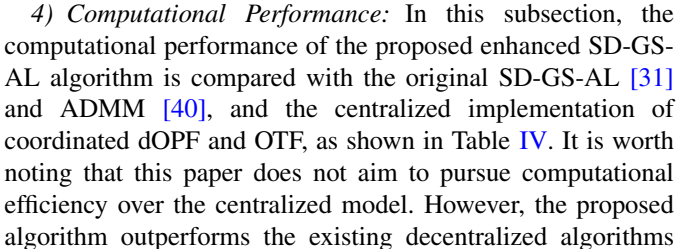


Fig. 8. Comparison of the boundary error (i.e., the difference of boundary variables) of the proposed enhanced SD-GS-AL algorithm, the original SD-GS-AL algorithm (with one inner loop iteration), and the ADMM (the ADMM convergence error is scaled down by a factor of 10) (Case 2).





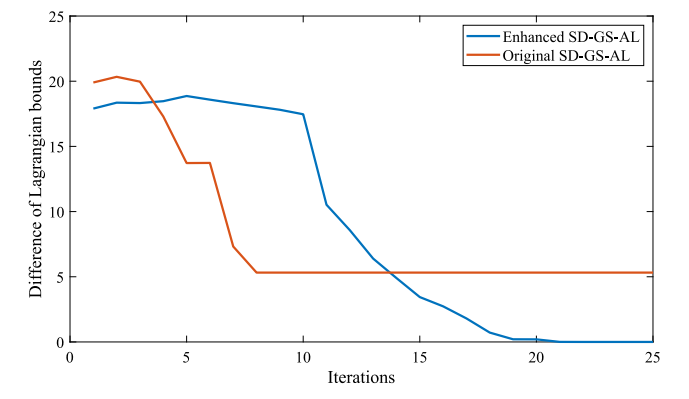


Fig. 9. Comparison of the convergence error (i.e., the difference of Lagrangian bounds) of the proposed enhanced SD-GS-AL algorithm and the original SD-GS-AL algorithm (with one inner loop iteration) (Case 3).

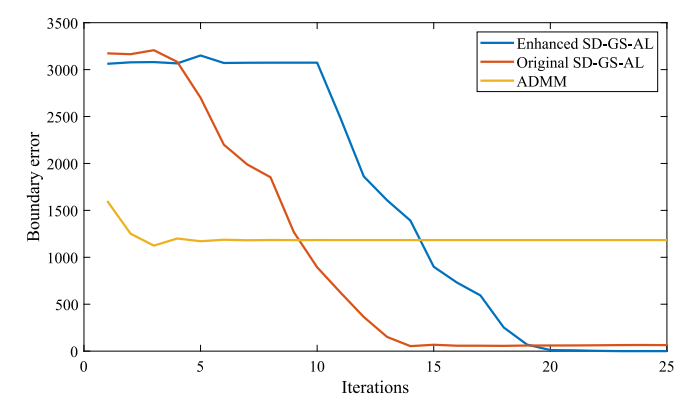


Fig. 10. Comparison of the boundary error (i.e., the difference of boundary variables) of the proposed enhanced SD-GS-AL algorithm, the original SD-GS-AL algorithm (with one inner loop iteration), and the ADMM (Case 3).

with similar features. For example, in Case 1, the original SD-GS-AL (with one inner loop iteration) and ADMM failed to converge. However, with eight inner loop iterations, the original SD-GS-AL converged in 13 outer iterations compared to 10 outer iterations of the proposed enhanced SD-GS-AL

O-D pair	Path (flow)	O-D pair	Path (flow)
1→4	$1 \to 2 \to 3 \to 4 (7)$	4→1	$4\rightarrow 3\rightarrow 2\rightarrow 1 (7)$
1 /4	$1\rightarrow \textcircled{5}\rightarrow 4$ (23)	7 /1	$4 \rightarrow 5 \rightarrow 1 (23)$

TABLE VI CHARGING AND ROUTING OF EVS (CASE 2)

O-D pair	Path (flow)	
1→2	$1 \rightarrow 5 \rightarrow 6 \rightarrow \bigcirc \rightarrow 8 \rightarrow 2 (60)$	
$4\rightarrow 2$	$4 \rightarrow 5 \rightarrow \textcircled{6} \rightarrow \textcircled{7} \rightarrow 8 \rightarrow 2 (60)$	
1→3	$1 \to 5 \to 6 \to 6 \to 11 \to 3 (60)$	
4→3	$4\rightarrow \mathfrak{G}\rightarrow \mathfrak{G}\rightarrow 11\rightarrow 3 (60)$	

algorithm, as shown in Table IV. Nonetheless, the original SD-GS-AL required more than three times more inner loop iterations (104 total inner loop iterations) than the proposed enhanced SD-GS-AL algorithm (28 total inner loop iterations). Similarly, in Cases 2 and 3, the proposed enhanced SD-GS-AL algorithm outperformed the original SD-GS-AL algorithm and ADMM. For a larger test case, i.e., Case 3, the computational improvement realized from the enhanced SD-GS-AL algorithm is even bigger. For example, with the enhanced SD-GS-AL, the number of inner loop iterations required is 80 compared to the 468 inner loop iterations required by the original SD-GS-AL. It is worth noting that the ADMM did not converge for all three test cases considered in this paper. Moreover, the proposed algorithm converged to the solutions of the centralized implementation of coordinated dOPF and OTF, as shown in Table IV.

# C. Engineering Validation of the Simulation Results

In this subsection, the engineering validation of the simulation results is made.

1) EVs Path, Path Flows, and EVs Charging: In this subsection, we provide optimal paths to route EVs and corresponding path flows and charging nodes for EVs in TN for all test cases. Table V provides the routing and charging of EVs along with the path flow for Case 1. For example, for the O-D pair 1-4, 7 EVs are routed on path  $1\rightarrow \bigcirc \rightarrow 4$ . Note that the circled node number indicates where the EVs are recharged. Similarly, Table VI provides the routing and charging of EVs along with the path flow for Case 2. The routing and charging of EVs with path flows for Case 3 will be discussed next when we discuss the implications of PDN-TN coordination on EVs flows.

2) Implications of PDN-TN Coordination on EV Flows: This subsection illustrates the implications of PDN-TN coordination on EV flows through comparative analysis. For comparison, three scenarios are considered: 1) EVs flows without PDN-TN coordination, 2) EVs flows with PDN-TN coordination using grid prices provided in Table I, and 3) EVs flows with PDN-TN coordination using congested grid prices. For the third scenario, we adjust the grid price of one feeder to simulate congested grid prices. Subsequent simulations allow

TABLE VII
EVS FLOWS ILLUSTRATING PDN-TN COORDINATION
WITH DIFFERENT GRID PRICES (CASE 3)

	O-D pair	Path (flow)
Scenario-1: No PDN-TN coordination	$1\rightarrow 20$	$1 \rightarrow 3 \rightarrow 4 \rightarrow \textcircled{5} \rightarrow 8 \rightarrow 16 \rightarrow 17 \rightarrow 19 \rightarrow 20 (60)$
	$2\rightarrow$ 13	$2 \rightarrow 6 \rightarrow \textcircled{5} \rightarrow 4 \rightarrow 3 \rightarrow 12 \rightarrow 13 (60)$
	3→19	$3 \rightarrow 4 \rightarrow 5 \rightarrow 9 \rightarrow 10 \rightarrow \text{(5)} \rightarrow 17 \rightarrow 19 \text{ (4)}$
		$3 \rightarrow 4 \rightarrow 11 \rightarrow 14 \rightarrow \cancel{(5)} \rightarrow 19 (45)$
		$3 \rightarrow 12 \rightarrow 11 \rightarrow 14 \rightarrow (5 \rightarrow 19 (11)$
	4→18	$4 \rightarrow 5 \rightarrow 6 \rightarrow 8 \rightarrow 7 \rightarrow 18 (60)$
	12→7	$12 \rightarrow \bigcirc \bigcirc \rightarrow 10 \rightarrow 16 \rightarrow 18 \rightarrow 7 (36)$
	23→6	$23 \rightarrow 14 \rightarrow \bigcirc \rightarrow 4 \rightarrow 5 \rightarrow 6 (60)$
Scenario-2: Coordination with normal grid prices	1→20	$1 \rightarrow 3 \rightarrow 4 \rightarrow \text{\textcircled{5}} \rightarrow 8 \rightarrow 16 \rightarrow 17 \rightarrow 19 \rightarrow 20 \tag{60}$
	2→13	$2 \rightarrow 6 \rightarrow (5) \rightarrow 4 \rightarrow 3 \rightarrow 12 \rightarrow 13 (60)$
	3→19	$3 \rightarrow 4 \rightarrow 5 \rightarrow 6 \rightarrow 8 \rightarrow \cancel{10} \rightarrow 17 \rightarrow 19 (44)$
		$3 \rightarrow 4 \rightarrow 11 \rightarrow 14 \rightarrow \textcircled{5} \rightarrow 19 (5)$
		$3 \rightarrow 12 \rightarrow 11 \rightarrow 14 \rightarrow \textcircled{5} \rightarrow 19 (11)$
	4→18	$4 \rightarrow 5 \rightarrow 6 \rightarrow 8 \rightarrow 7 \rightarrow 18 (60)$
	12→7	$12 \rightarrow 3 \rightarrow 4 \rightarrow (5) \rightarrow 6 \rightarrow 8 \rightarrow 7 (24)$
		$12 \rightarrow \bigcirc \bigcirc \rightarrow 10 \rightarrow 16 \rightarrow 18 \rightarrow 7 (36)$
	23→6	$23 \rightarrow 14 \rightarrow \bigcirc \rightarrow 4 \rightarrow 5 \rightarrow 6 (53)$
		$23 \rightarrow 22 \rightarrow \cancel{(5)} \rightarrow 19 \rightarrow 17 \rightarrow 16 \rightarrow 8 \rightarrow 6 (7)$
Scenario-3: Coordination with congested grid prices	$1\rightarrow 20$	$1 \rightarrow 3 \rightarrow 4 \rightarrow \textcircled{5} \rightarrow 8 \rightarrow 16 \rightarrow 17 \rightarrow 19 \rightarrow 20 (60)$
	2→13	$2 \rightarrow 6 \rightarrow (5) \rightarrow 4 \rightarrow 3 \rightarrow 12 \rightarrow 13 (60)$
	3→19	$3 \rightarrow 4 \rightarrow 5 \rightarrow 6 \rightarrow 8 \rightarrow \cancel{16} \rightarrow 17 \rightarrow 19 (20)$
		$3 \to 4 \to 11 \to 14 \to (5 \to 19 (23)$
		$3 \rightarrow 12 \rightarrow 11 \rightarrow 14 \rightarrow (5 \rightarrow 19 (17)$
	4→18	$4 \rightarrow 5 \rightarrow 6 \rightarrow 8 \rightarrow 7 \rightarrow 18 (60)$
	12→7	$12 \rightarrow 3 \rightarrow 4 \rightarrow \text{\textcircled{5}} \rightarrow 6 \rightarrow 8 \rightarrow 7 \tag{22}$
		$12 \rightarrow \bigcirc \bigcirc \rightarrow 10 \rightarrow 16 \rightarrow 18 \rightarrow 7 (38)$
		$23 \rightarrow 14 \rightarrow \bigcirc \rightarrow 4 \rightarrow 5 \rightarrow 6 (60)$

us to analyze and compare the changes in EV flows. It should be noted that the grid prices referred to in Table I represent the Locational Marginal Prices (LMPs) in the power transmission system (PTS). During congestion in parts of the PTS, the LMPs (also called grid prices in this paper) at affected buses surge markedly, setting them apart from the rest of the system. Therefore, to simulate congested grid prices, the grid price of Feeder 4 is changed from \$91.62 to \$140.94. The rest of the grid prices are left unchanged.

For brevity, we only consider Case 3 in the comparative analysis. Table VII shows the results of the comparison, which shows variations in the routing and charging of EVs across different coordination scenarios. Notably, EV traffic is reduced on routes supplied by congested grid prices compared to those with normal pricing. For example, for O-D pair  $3\rightarrow19$ , the first path  $3\rightarrow4\rightarrow5\rightarrow6\rightarrow8\rightarrow(\cancel{5}\rightarrow17\rightarrow19$  routes 44 out of 60 EVs in normal grid price condition (scenario 2). However, in the congested grid price scenario (scenario 3), the same path carries less than half the number of EVs (i.e., 20). It is worth noting that the congested feeder supplies the EVCS located at node 16 on this path. Therefore, fewer EVs were routed through this path in the congested scenario. This highlights the importance of PDN-TN coordination in the face of rising EV charging.

3) Distribution-Level Optimal Power Flow Results: This subsection presents nodal voltage profiles of feeders across all

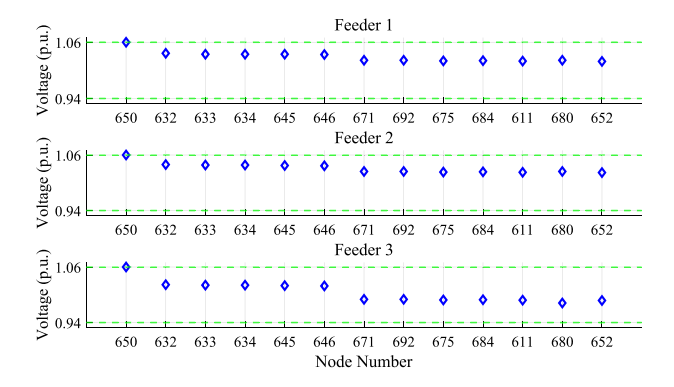


Fig. 11. Nodal voltage profile (Case 1).

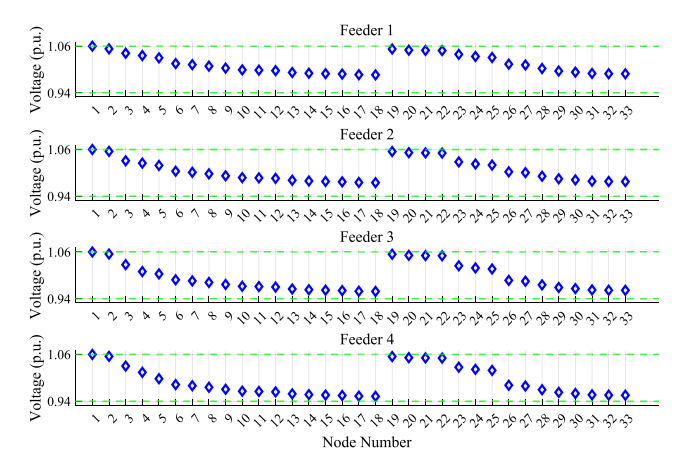


Fig. 12. Nodal voltage profile (Case 2).

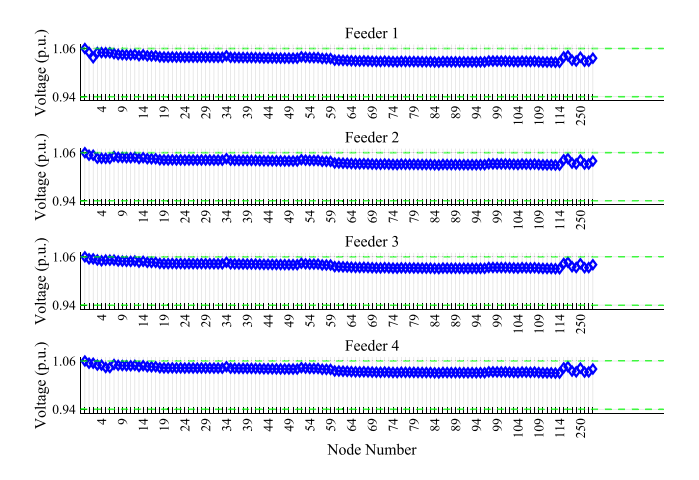


Fig. 13. Nodal voltage profile (Case 3).

three different test cases. Figures 11, 12, and 13 illustrate that the nodal voltages for the feeders in each test case remain within the specified limits (0.94 p.u. - 1.06 p.u.) Nonetheless, from the Figures, we can observe that the EVCS operation in TN has some impact on the voltage profile in the feeder. For example, Feeder 3 supplies the EVCS at node 5 in TN in Case 1 (shown in Figure 2). As seen from Table V, most of the EV traffic (46 (23+23) out of 60) gets charged at node 5. Therefore, the nodal voltage profile of Feeder 3 (which supplies EVCS at node 5 in TN) is lower than the voltage profile of the other two feeders, as seen from Figure 11.

Nonetheless, the voltage profile of all feeders across three test cases is within the acceptable operation limits.

#### V. CONCLUSION

This paper presents an enhanced SD-GS-AL decentralized algorithm for coordinating PDN and TN with EVs. In comparison to existing methods, the main benefits of the proposed algorithm are: 1) unlike existing algorithms like ADMM, it is applicable to MIP problems with convergence and optimality guaranteed; 2) it only requires limited information exchange between PDN and TN operators, which will help preserve the privacy of the two systems and reduce the investment in building communication channels, 3) it is fully decentralized so that all the computations are carried out by PDN operator and TN coordinator only (in parallel), 4) it is faster than the original SD-GS-AL [31]. The simulation results showed the significance of the proposed framework and algorithm over the existing ones.

# REFERENCES

- [1] T. Bunsen et al., Global EV Outlook 2018: Towards Cross-Modal Electrification. Paris, France: Int. Energy Agency, 2018.
- [2] W. Wei, S. Mei, L. Wu, M. Shahidehpour, and Y. Fang, "Optimal traffic-power flow in urban electrified transportation networks," *IEEE Trans. Smart Grid*, vol. 8, no. 1, pp. 84–95, Jan. 2017.
- [3] S. Lv, Z. Wei, G. Sun, S. Chen, and H. Zang, "Optimal power and semi-dynamic traffic flow in urban electrified transportation networks," *IEEE Trans. Smart Grid*, vol. 11, no. 3, pp. 1854–1865, May 2020.
- [4] X. Shi, Y. Xu, Q. Guo, and H. Sun, "Optimal dispatch based on aggregated operation region of EV considering spatio-temporal distribution," *IEEE Trans. Sustain. Energy*, vol. 13, no. 2, pp. 715–731, Apr. 2022.
- [5] S. Lai, J. Qiu, Y. Tao, and J. Zhao, "Pricing strategy for energy supplement services of hybrid electric vehicles considering boundedrationality and energy substitution effect," *IEEE Trans. Smart Grid*, vol. 14, no. 4, pp. 2973–2985, Jul. 2023.
- [6] S. Lai, J. Qiu, Y. Tao, and J. Zhao, "Pricing for electric vehicle charging stations based on the responsiveness of demand," *IEEE Trans. Smart Grid*, vol. 14, no. 1, pp. 530–544, Jan. 2023.
- [7] Q. Li, R. Ayyanar, and V. Vittal, "Convex optimization for DES planning and operation in radial distribution systems with high penetration of photovoltaic resources," *IEEE Trans. Sustain. Energy*, vol. 7, no. 3, pp. 985–995, Jul. 2016.
- [8] W. Wei, L. Wu, J. Wang, and S. Mei, "Network equilibrium of coupled transportation and power distribution systems," *IEEE Trans. Smart Grid*, vol. 9, no. 6, pp. 6764–6779, Nov. 2018.
- [9] G. Sun, G. Li, P. Li, S. Xia, Z. Zhu, and M. Shahidehpour, "Coordinated operation of hydrogen-integrated urban transportation and power distribution networks considering fuel cell electric vehicles," *IEEE Trans. Ind. Appl.*, vol. 58, no. 2, pp. 2652–2665, Mar./Apr. 2022.
- [10] T. Zhao, H. Yan, X. Liu, and Z. Ding, "Congestion-aware dynamic optimal traffic power flow in coupled transportation power systems," *IEEE Trans. Ind. Informat.*, vol. 19, no. 2, pp. 1833–1843, Feb. 2023.
- [11] Y. Zhang, S. Xie, and S. Shu, "Decentralized optimization of multiarea interconnected traffic-power systems with wind power uncertainty," *IEEE Trans. Ind. Informat.*, vol. 19, no. 1, pp. 133–143, Jan. 2023.
- [12] Y. Sun, Z. Chen, Z. Li, W. Tian, and M. Shahidehpour, "EV charging schedule in coupled constrained networks of transportation and power system," *IEEE Trans. Smart Grid*, vol. 10, no. 5, pp. 4706–4716, Sep. 2019.
- [13] G. Sun, G. Li, S. Xia, M. Shahidehpour, X. Lu, and K. W. Chan, "ALADIN-based coordinated operation of power distribution and traffic networks with electric vehicles," *IEEE Trans. Ind. Appl.*, vol. 56, no. 5, pp. 5944–5954, Sep./Oct. 2020.
- [14] S. Xie, Y. Xu, and X. Zheng, "On dynamic network equilibrium of a coupled power and transportation network," *IEEE Trans. Smart Grid*, vol. 13, no. 2, pp. 1398–1411, Mar. 2022.

- [15] W. Qiao, Y. Han, Q. Zhao, F. Si, and J. Wang, "A distributed coordination method for coupled traffic-power network equilibrium incorporating behavioral theory," *IEEE Trans. Veh. Technol.*, vol. 71, no. 12, pp. 12588–12601, Dec. 2022.
- [16] K. Li, C. Shao, H. Zhang, and X. Wang, "Strategic pricing of electric vehicle charging service providers in coupled power-transportation networks," *IEEE Trans. Smart Grid*, vol. 14, no. 3, pp. 2189–2201, May 2023.
- [17] C. Shao, K. Li, T. Qian, M. Shahidehpour, and X. Wang, "Generalized user equilibrium for coordination of coupled power-transportation network," *IEEE Trans. Smart Grid*, vol. 14, no. 3, pp. 2140–2151, May 2023.
- [18] S. Xie, Q. Wu, N. D. Hatziargyriou, M. Zhang, Y. Zhang, and Y. Xu, "Collaborative pricing in a power-transportation coupled network: A variational inequality approach," *IEEE Trans. Power Syst.*, vol. 38, no. 1, pp. 783–795, Jan. 2023.
- [19] H. Zhang, Z. Hu, and Y. Song, "Power and transport nexus: Routing electric vehicles to promote renewable power integration," *IEEE Trans. Smart Grid*, vol. 11, no. 4, pp. 3291–3301, Jul. 2020.
- [20] X. Shi, Y. Xu, Q. Guo, H. Sun, and W. Gu, "A distributed EV navigation strategy considering the interaction between power system and traffic network," *IEEE Trans. Smart Grid*, vol. 11, no. 4, pp. 3545–3557, Jul. 2020.
- [21] M. B. Tookanlou, S. A. P. Kani, and M. Marzband, "An optimal day-ahead scheduling framework for E-mobility ecosystem operation with drivers' preferences," *IEEE Trans. Power Syst.*, vol. 36, no. 6, pp. 5245–5257, Nov. 2021.
- [22] B. Sohet, Y. Hayel, O. Beaude, and A. Jeandin, "Hierarchical coupled driving-and-charging model of electric vehicles, stations and grid operators," *IEEE Trans. Smart Grid*, vol. 12, no. 6, pp. 5146–5157, Nov. 2021.
- [23] T. Qian, C. Shao, X. Li, X. Wang, Z. Chen, and M. Shahidehpour, "Multi-agent deep reinforcement learning method for EV charging station game," *IEEE Trans. Power Syst.*, vol. 37, no. 3, pp. 1682–1694, May 2022.
- [24] J. Liu, G. Lin, S. Huang, Y. Zhou, C. Rehtanz, and Y. Li, "Collaborative EV routing and charging scheduling with power distribution and traffic networks interaction," *IEEE Trans. Power Syst.*, vol. 37, no. 5, pp. 3923–3936, Sep. 2022.
- [25] S. Chen, S. Feng, Z. Guo, and Z. Yang, "Trilevel optimization model for competitive pricing of electric vehicle charging station considering distribution locational marginal price," *IEEE Trans. Smart Grid*, vol. 13, no. 6, pp. 4716–4729, Nov. 2022.
- [26] Q. Nguyen, H. V. Padullaparti, K.-W. Lao, S. Santoso, X. Ke, and N. Samaan, "Exact optimal power dispatch in unbalanced distribution systems with high PV penetration," *IEEE Trans. Power Syst.*, vol. 34, no. 1, pp. 718–728, Jan. 2019.

- [27] D. K. Molzahn et al., "A survey of distributed optimization and control algorithms for electric power systems," *IEEE Trans. Smart Grid*, vol. 8, no. 6, pp. 2941–2962, Nov. 2017.
- [28] N. Michelena, H. Park, and P. Y. Papalambros, "Convergence properties of analytical target cascading," AIAA J., vol. 41, no. 5, pp. 897–905, 2003.
- [29] A. Losi and M. Russo, "On the application of the auxiliary problem principle," J. Optim. Theory Appl., vol. 117, no. 2, pp. 377–396, 2003.
- [30] M. Kraning, E. Chu, J. Lavaei, and S. Boyd, "Dynamic network energy management via proximal message passing," Found. Trends Optim., vol. 1, no. 2, pp. 73–126, 2014, doi: 10.1561/2400000002.
- [31] N. Boland, J. Christiansen, B. Dandurand, A. Eberhard, and F. Oliveira, "A parallelizable augmented lagrangian method applied to large-scale non-convex-constrained optimization problems," *Math. Program.*, vol. 175, no. 1, pp. 503–536, 2019.
- [32] Q. Li, S. Yu, A. S. Al-Sumaiti, and K. Turitsyn, "Micro water-energy nexus: Optimal demand-side management and quasi-convex hull relaxation," *IEEE Trans. Control Netw. Syst.*, vol. 6, no. 4, pp. 1313–1322, Dec. 2019.
- [33] Y. Cui, Z. Hu, and X. Duan, "Optimal pricing of public electric vehicle charging stations considering operations of coupled transportation and power systems," *IEEE Trans. Smart Grid*, vol. 12, no. 4, pp. 3278–3288, Jul. 2021.
- [34] J. G. Wardrop, "Road paper. some theoretical aspects of road traffic research," *Proc. Instit. Civil Eng.*, vol. 1, no. 3, pp. 325–362, 1952, doi: 10.1680/ipeds.1952.11259.
- [35] Q. Li and V. Vittal, "Convex hull of the quadratic branch AC power flow equations and its application in radial distribution networks," *IEEE Trans. Power Syst.*, vol. 33, no. 1, pp. 839–850, Jan. 2018.
- [36] E. M. L. Beale and J. A. Tomlin, "Special facilities in a general mathematical programming system for non-convex problems using ordered sets of variables," *Oper. Res.*, vol. 69, nos. 447-454, p. 99, 1970
- [37] R. Glowinski and P. Le Tallec, Augmented Lagrangian and Operator-Splitting Methods in Nonlinear Mechanics. Philadelphia, PA, USA: SIAM, 1989.
- [38] M. Lubin, K. Martin, C. G. Petra, and B. Sandıkçı, "On parallelizing dual decomposition in stochastic integer programming," *Oper. Res. Lett.*, vol. 41, no. 3, pp. 252–258, May 2013.
- [39] S. V. Ukkusuri and W. F. Yushimito, "A methodology to assess the criticality of highway transportation networks," *J. Transp. Secur.*, vol. 2, pp. 29–46, May 2009.
- [40] S. Boyd, N. Parikh, and E. Chu, "Distributed optimization and statistical learning via the alternating direction method of multipliers," *Found. Trends Mach. Learn.*, vol. 3, no. 1, pp. 1–122, 2011.